Climate
of the Past

Precipitation δ^{18}O on the Himalaya–Tibet orogeny and its relationship to surface elevation

Hong Shen and Christopher J. Poulsen

Department of Earth and Environmental Sciences, University of Michigan, Ann Arbor, 48109, USA

Correspondence: Hong Shen (hdshen@umich.edu)

Abstract. The elevation history of the Himalaya–Tibet orogen is central to understanding the evolution and dynamics of both the India–Asia collision and the Asian monsoons. The surface elevation history of the region is largely deduced from stable isotope (δ^{18}O, δD) paleoaltimetry. This method is based on the observed relationship between the isotopic composition of meteoric waters (δ^{18}O$_p$, δD$_p$) and surface elevation, and the assumption that precipitation undergoes Rayleigh distillation under forced ascent. Here we evaluate how elevation-induced climate change influences the δ^{18}O$_p$–elevation relationship and whether Rayleigh distillation is the dominant process affecting δ^{18}O$_p$. We use an isotope-enabled climate model, ECHAM-wiso, to show that the Rayleigh distillation process is only dominant in the monsoonal regions of the Himalayas when the mountains are high. When the orogen is lowered, local surface recycling and convective processes become important, as forced ascent is weakened due to weaker Asian monsoons. As a result, the δ^{18}O$_p$ lapse rate in the Himalayas increases from around -3 to above -0.1‰ km^{-1}, and has little relationship with elevation. On the Tibetan Plateau, the meridional gradient of δ^{18}O decreases from ~ 1 to ~ 0.3‰ $^\circ$$^{-1}$ with reduced elevation, primarily due to enhanced sub-cloud reevaporation under lower relative humidity. Overall, we report that using δ^{18}O$_p$ or δD$_p$ to deduce surface elevation change in the Himalayan–Tibetan region has severe limitations and demonstrate that the processes that control annual-mean precipitation-weighted δ^{18}O$_p$ vary by region and with surface elevation. In summary, we determine that the application of δ^{18}O paleoaltimetry is only appropriate for 7 of the 50 sites from which δ^{18}O records have been used to infer past elevations.

1 Introduction

Surface elevation is a fundamental characteristic of the Earth surface, directly affecting atmospheric circulation patterns and surface temperatures, precipitation and surface hydrology, erosion and sediment transport, and the distribution and diversity of life (Aron and Poulsen, 2018). The evolution of surface elevation resulting from the India–Asia convergence and the creation of the Himalaya–Tibet orogen was the defining event of the Asian continent in the Cenozoic and had global environmental implications. Surface uplift of the orogen has been implicated in the onset and strengthening of the southeast Asian monsoon system (Boos and Kuang, 2010; Zhang et al., 2015) and the position of atmospheric stationary waves (Kutzbach et al., 1989), the evolutionary diversification and biogeographic distribution of fauna and flora in central Asia (Zhao et al., 2016; Yang et al., 2009; Antonelli et al., 2018), and the intensification of chemical weathering of exposed rocks and transport of nutrients to the ocean that contributed to the global atmospheric CO_2 drawdown (Galy et al., 2007; Maffre et al., 2018). Surface elevation also lends a first-order constraint on the crustal and upper mantle dynamics that create topography (Ehlers and Poulsen, 2009). Surface elevation estimates for the Himalaya–Tibet orogen, and specifically evidence for high elevations of the orogen since the late Eocene, have been instrumental in supporting geodynamical models of Tibetan Plateau growth through early deformation and crustal thickening (Rowley and Currie, 2006; Rohrmann et al., 2012; Hoke et al., 2014).

The paramount importance of surface elevation to our understanding of Cenozoic environmental and tectonic evolution has led to a proliferation of studies that infer past Himalayan–Tibetan surface elevations from ancient proxy

materials (Cyr et al., 2005; Rowley and Currie, 2006; Li et al., 2015). Stable isotope paleoaltimetry, one of the few quantitative methods to reconstruct past surface elevations, relies on the water isotopic composition of ancient materials, including pedogenic and lacustrine carbonates, authigenic clay and hydrated volcanic glass, which were formed in contact with ancient surface waters. The method is predicated on the observed, modern decrease in water stable isotopic compositions (δ^{18}O, δD) with elevation gain (the isotopic lapse rate) (Chamberlain and Poage, 2000), a relationship that is commonly attributed to the rainout of heavy isotopologues during the stably forced ascent of a saturated air parcel over high elevation and is modeled as a Rayleigh distillation process (e.g., Rowley and Garzione, 2007). Stable isotope paleoaltimetry has been used to reconstruct past surface elevation of many of the world's major mountain belts, including the North American Cordillera (e.g., Poage and Chamberlain, 2002; Fan et al., 2014), the Andes (e.g., Garzione et al., 2008), and the Himalayan–Tibetan orogen (e.g., Rowley and Currie, 2006), due to the robustness of the isotopic lapse rate in modern orogenic regions and the ubiquity of proxy materials.

The interpretation of stable isotopes in ancient materials to infer past surface elevation is complicated by factors related to both the mineralization of proxy materials and the isotope–elevation relationship of meteoric waters from which the proxies form (Poage and Chamberlain, 2001). With regard to the latter factor, studies using global climate models have demonstrated that the isotopic lapse rate can be dependent on a mountain range's elevation due to processes that are not described by Rayleigh distillation (Ehlers and Poulsen, 2009; Poulsen et al., 2010; Feng et al., 2013; Botsyun et al., 2016). Indeed, Feng et al. (2013) showed that the simulated δ^{18}O of precipitation (δ^{18}O$_p$) during the uplift of the Eocene North American Cordillera was substantially influenced by changes in vapor mixing, surface recycling, moisture source change, and precipitation type. Similarly, Botsyun et al. (2016) investigated δ^{18}O$_p$ across the Himalayan–Tibetan region in response to surface uplift and showed that direct topographic effects only partially accounted for total δ^{18}O$_p$ changes.

On the Himalayan slope, δ^{18}O in surface waters and precipitation has been widely observed to decrease with elevation at a rate of $\sim 3\,\%_o\,\mathrm{km}^{-1}$ (e.g., Rowley et al., 2001). The δ^{18}O–elevation relationship has been attributed to orographic rainout and modeled as a Rayleigh distillation process (e.g., Rowley and Currie, 2006). On the Tibetan Plateau, δ^{18}O in surface water and precipitation increases linearly with latitude by $\sim 1\,\%_o\,^{\circ-1}$ over nearly uniform elevation (e.g., Bershaw et al., 2012). The source of δ^{18}O variations on the plateau and whether δ^{18}O can be used for paleoaltimetry on the high Tibetan Plateau has received little attention. Quade et al. (2011) proposed that paleoelevations could be inferred from proxy δ^{18}O after removing the meridional δ^{18}O gradient on the Tibetan Plateau. This south-to-north gradient in δ^{18}O has been reported to have existed since the early Eocene

(Caves Rugenstein and Chamberlain, 2018). However, little is known about the processes that contribute to the meridional δ^{18}O gradient or how the meridional δ^{18}O gradient varied when the plateau was lower.

The goal of this study is to identify and quantify the processes that control δ^{18}O$_p$ variations across the Himalayas and the Tibetan Plateau and to evaluate the utility of δ^{18}O$_p$ as a paleoaltimeter in these regions. To do this, we use an isotope-enabled global climate model, ECHAM5-wiso, with prescribed elevation scenarios and compare the annual-mean precipitation-weighted δ^{18}O$_p$ calculated by the climate model with that expected due to Rayleigh distillation alone. Botsyun et al. (2016) used the LMDZ-iso model to decompose the influence of adiabatic elevation changes on δ^{18}O$_p$ from other influences due to nonadiabatic temperature changes, local changes in relative humidity, and post-condensational processes. Building on Botsyun et al. (2016), we take a more process-oriented approach to quantify the isotopic fluxes attributed to specific mechanisms and demonstrate that the contributions from these processes vary spatially and in response to elevation change. Finally, we discuss the implications of our results for reconstructing paleoaltimetry of the Himalayas and Tibetan Plateau.

2 Methods

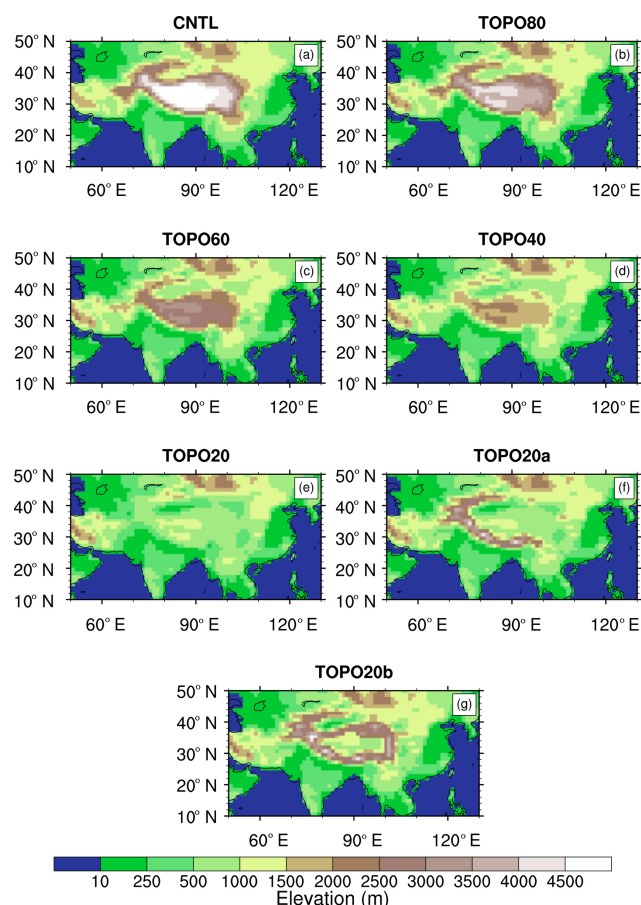### 2.1 Model and experimental design

In this study, we employ ECHAM5-wiso, a water isotope-enabled atmospheric global climate model (AGCM). The model has been widely used for both modern and past climate and isotope simulations. For instance, Feng et al. (2013) and Feng and Poulsen (2016) employed ECHAM5-wiso to explore climate and isotopic responses to Cenozoic surface uplift and climate change in western North America. ECHAM has also been shown to simulate many aspects of Asian climate (e.g., Battisti et al., 2014), and isotopic compositions (δ^{18}O$_p$) simulated by ECHAM5-wiso generally agree well with observed modern stream and precipitation δ^{18}O across the Tibetan Plateau as shown by Li et al. (2016; see their Fig. 11).

We use a model configuration with 19 vertical levels, and a spectral triangular truncation of 106 horizontal waves, approximately equivalent to a 100 km grid spacing. This horizontal resolution, although still relatively coarse, is about twice that of recent simulations used to validate the simulation of water isotopes over the Tibetan Plateau (Li et al., 2016) and recent paleoclimate simulations of the region (e.g., Roe et al., 2016). The AGCM is coupled to a slab ocean model, the MPI-OM, with prescribed ocean heat flux from the Atmospheric Modeling Project Intercomparison 2 (AMIP2; Gleckler, 2005) averaged over the years from 1956 to 2000. A modern annual mean seawater δ^{18}O dataset spanning from 1956 to 2006 (LeGrande and Schmidt, 2006) is provided as a lower boundary condition for the model.

In ECHAM5-wiso, water isotopologues are included as independent tracers in the atmosphere. When water evaporates from the sea, both equilibrium and nonequilibrium distillation processes occur as a function of sea-surface temperature, wind speed, relative humidity, isotope composition in seawater, and vapor above the ocean surface (Hoffmann et al., 1998). Convective rains are assumed to have larger raindrops that reach only partial (50 %) isotopic equilibrium with the surrounding vapor, whereas large-scale precipitation has smaller raindrops and attains almost complete (90 %) equilibrium with the environment (Hoffmann et al., 1998). For kinetic fractionation of raindrops during partial evaporation in ECHAM5-wiso, the fractionation factor is formulated to depend on the sub-cloud relative humidity of the entire grid box (Hoffmann et al., 1998). Only large lakes, the size of at least one-half grid cell, are resolved in the model, and fractionation from the land surface is not included as its impact on precipitation $\delta^{18}O_p$ is negligible (Haese et al., 2013).

We conducted two sets of sensitivity experiments (Fig. 1) in addition to a control simulation with modern conditions (CNTL). In the first set of sensitivity experiments, topography is uniformly lowered to 80 % (TOPO80), 60 % (TOPO60), 40 % (TOPO40), and 20 % (TOPO20) of its modern elevation over a domain that includes the Himalayas and the Tibetan Plateau. In the second set of sensitivity experiments, we conducted two experiments with nonuniform elevation modifications over this domain. The first experiment includes a high Himalayan front with the Tibetan Plateau reduced to 20 % of its modern elevation (TOPO20a). This experiment is inspired by the widely accepted notion that southeast Asia had an Andean type mountain belt before the collision of the Eurasian and Indian plates (Royden et al., 2008). TOPO20a also serves as a test of the Himalayas on the regional climate. In the second experiment, the outer edge of the Tibetan Plateau remains, but the inside is lowered to 20 % of its modern height (TOPO20b). The second experiment is a sensitivity test to investigate the role of plateau heating on regional climate and isotopic compositions. In both sets of experiments, we tapered the topography along the borders of the domains to avoid any abrupt topography boundaries. Except for topography, all other boundary conditions were kept the same among all experiments. Each experiment was run for 20 years, with the last 15 years used for analysis. Summertime (June–July–August) climate variables and annual-mean precipitation-weighted δ^{18}O are analyzed and presented, reflecting that total precipitation over most of the region is dominated by summer precipitation and that carbonates preferentially form in summer when precipitation peaks (Peters et al., 2013).

Mean climate conditions today vary across the Himalaya; the western Himalaya is characterized by peak precipitation in winter and early spring, while the central Himalaya is dominated by the Indian summer monsoon (IM) and the eastern Himalayas are dominated by the East Asia summer monsoon (EASM) (Yao et al., 2013). Because of this het-
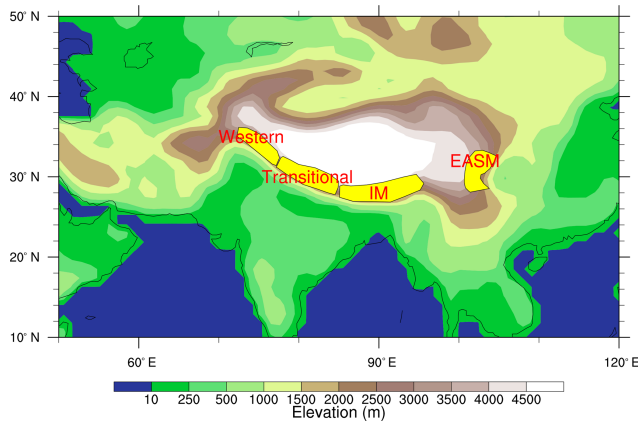

Figure 1. Surface elevations (m) prescribed in the ECHAM5 **(a)** CNTL, **(b)** TOPO80, **(c)** TOPO60, **(d)** TOPO40, **(e)** TOPO20, **(f)** TOPO20a, and **(g)** TOPO20b cases. Note that the CNTL simulation includes modern elevations. The names of the other cases (e.g., TOPO60) indicate the surface elevation of the Himalayan–Tibetan region relative to the modern elevation (e.g., 60 %). Cases TOPO2a and TOPO20b are modifications of the TOPO20 case (see Sect. 2).

erogeneity, we separate the Himalayas into four distinct regions for analysis purposes: the western Himalayas; a transitional area between western and central Himalayas; central Himalayas; and eastern Himalayas (the transitional areas between the central and eastern Himalayas are excluded because the climate and isotopic signals are similar to the IM and EASM regions). The strength and pattern of precipitation and wind, and isotopic compositions in the two eastern-most transitional areas are similar to those in the IM and EASM in most cases. Thus, in the following we only present results for the western, transitional, IM, and EASM regions as shown in Fig. 2.

2.2 Rayleigh distillation

We developed an open-system, one-dimensional, altitude-dependent Rayleigh distillation model (RDM) in order to es-

Figure 2. Topographic map (m) showing the Himalayan climate zones following Yao et al. (2013). Western, transitional, Indian summer monsoon (IM), and Eastern Asian summer monsoon (EASM) regions are marked. Transitional areas between the central and eastern Himalayas are excluded because the climate and isotopic signals are similar to the IM and EASM regions.

timate decreases in $\delta^{18}O_p$ due to Rayleigh distillation during ascent. The RDM tracks the isotopic composition of an air parcel as it ascends adiabatically from low to high altitude, becomes saturated, and loses condensate through precipitation. In the RDM, an air parcel cools at the dry adiabatic lapse rate before condensation and at the moist adiabatic lapse rate upon saturation (Rowley and Garzione, 2007). The RDM is run using terrain-following coordinates and is initialized with three different moisture sources: (1) fixed air temperature ($T = 20\,°C$) and relative humidity (RH $= 80\,\%$); (2) local, summertime low-level T and RH from ECHAM5; and (3) fixed $T = 20\,°C$ and summertime RH from ECHAM5. In this way, we are able to quantify the influence due to total moisture source change – (1) minus (2) – and further decompose this influence into the changes in T – (3) minus (2) – or RH – (1) minus (3).

In order to estimate how much of the mass flux of ^{18}O in total precipitation is contributed by the Rayleigh distillation process, we assumed that all large-scale precipitation, P_l, forms in response to stable upslope ascent and participates in Rayleigh distillation. We then estimated the isotopic flux of water undergoing Rayleigh distillation as follows:

$$\mathrm{RD} = \left(\frac{\delta^{18}O_{\mathrm{RDM}}}{1000} + 1 \right) R_{\mathrm{vsmow}} \times P_l \times \rho_{\mathrm{water}}, \quad (1)$$

where RD has units of $g\,m^{-2}\,h^{-1}$, ρ_{water} (in $g\,m^{-3}$) is the density of water, P_l (in $m\,h^{-1}$) is the large-scale precipitation rate, and $\delta^{18}O_{\mathrm{RDM}}$ is the isotopic composition simulated by the RDM at the same elevation as the grid points in Sect. 2.3 where the mass flux in total precipitation is estimated. Note that this estimation of RD stands for the upper limit of the contribution of RD, as not all large-scale precipitation is triggered by the Rayleigh distillation process.

To compare the relative importance of Rayleigh distillation with other isotopic fractionation processes in ECHAM, we quantify the change in upslope $\delta^{18}O_p$ attributable to Rayleigh distillation. We do this by comparing the rate of upslope $\delta^{18}O_p$ change (hereafter referred to as the $\delta^{18}O_p$ lapse rates) in ECHAM with that estimated using the RDM. We define the $\delta^{18}O_p$ lapse rate as the slope of the linear regression equation of precipitation-weighted $\delta^{18}O_p$ regressed on elevation and use the coefficient of determination (R^2) of this regression to evaluate the robustness of the $\delta^{18}O_p$–elevation relationship. We use a ratio of the $\delta^{18}O_p$ lapse rate in ECHAM to that in the RDM (p_percent) to approximate the contribution of Rayleigh distillation to the ECHAM $\delta^{18}O_p$ lapse rate. When R^2 and p_percent are both above 0.5 for a particular domain and elevation scenario, we consider that the ECHAM $\delta^{18}O_p$ lapse rate agrees with the RDM $\delta^{18}O_p$ lapse rate.

$\delta^{18}O_p$ decreases as an air parcel travels inland. This continental effect may contribute to a significant portion of the decrease in $\delta^{18}O_p$ over elevated regions in the low-elevation scenarios. To evaluate whether a strong $\delta^{18}O_p$–elevation relationship exists in low-elevation scenarios, we examine the ratio of the slope of $\delta^{18}O_p$ regressed against latitude on the subcontinent to the south of the Himalayas to that on the Himalayan slope. This method accounts for the fact that $\delta^{18}O_p$ changes with both latitude and elevation. A significant $\delta^{18}O_p$–elevation relationship is signified by a large ratio, indicating that $\Delta\delta^{18}O_p$ with elevation is greater than that with latitude.

2.3 Quantifying effects through the mass flux of ^{18}O

Mass fluxes of ^{18}O are calculated to quantify the contribution of vapor mixing, surface recycling, and RDM to the ^{18}O in total precipitation. Vapor mixing and surface recycling serve as the lateral and lower boundary sources of ^{18}O in an air column, respectively, and total precipitation as the sink. Within this air column, sinks and sources of ^{18}O in the air are assumed to compensate for one another to make the total mass of ^{18}O in the air stable on climatological timescales, with the mass flux of ^{18}O from vapor mixing and surface recycling balancing that from total precipitation. With this compensation of sources and sinks in mind, we calculated the flux of ^{18}O due to vapor mixing, surface recycling, and total precipitation.

The vapor mixing between air masses is estimated as the advection of ^{18}O in a vertical air column:

$$\frac{\partial M^{18}O}{\partial t} \sim \int -\overline{V} \cdot \overline{\nabla} m^{18}O \mathrm{d}z, \quad (2)$$

where $M^{18}O$ ($g\,m^{-2}$) is the unit column-total mass of ^{18}O in the air, $\overline{V}$ ($m\,h^{-1}$) is the wind speed vector within a layer, $m^{18}O$ ($g\,m^{-3}$) is the mass of ^{18}O per m3 of air, and z (m) is elevation. Approximating the total mass of water by the amount of ^{16}O, $m^{18}O$ is defined in terms of $\delta^{18}O_c$ from Eq. (1) as

$$m^{18}O \approx q\rho_{air}\left(\frac{\delta^{18}O}{1000} + 1\right)R_{vsmow}. \tag{3}$$

By substituting $\delta^{18}O_c$ in Eq. (3) into Eq. (2), the final form of the total column-integrated vapor mixing ($g\,m^{-2}\,h^{-1}$) is written as

$$VM = \int -\overline{V} \cdot \overline{\nabla}m^{18}Odz = -\int \overline{V}$$
$$\cdot \overline{\nabla}\left[q\rho_{air}\left(\frac{\delta^{18}O}{1000} + 1\right)R_{vsmow}\right]\rho_{air}dz. \tag{4}$$

Note that the centered-finite-difference method is used in discretizing the derivatives in Eq. (4). This method could potentially introduce errors in comparison to the spectral method used in the dynamical core of ECHAM5.

Recycling of surface water vapor transports ^{18}O to the atmosphere from lower boundary. To estimate this contribution to ^{18}O, the recycled mass flux (in $g\,m^{-2}\,h^{-1}$) is calculated as follows:

$$\left(\frac{\delta^{18}O}{1000} + 1\right)R_{vsmow} \times E \times \rho_{water}, \tag{5}$$

where $\delta^{18}O$ is the isotopic composition of the evaporated water and E ($m\,h^{-1}$) is the surface evaporation rate.

The mass flux of ^{18}O in total precipitation is estimated in the following manner as per Eq. (3):

$$\left(\frac{\delta^{18}O}{1000} + 1\right)R_{vsmow} \times P \times \rho_{water}, \tag{6}$$

where $\delta^{18}O$ is the isotopic composition of precipitation and P ($m\,h^{-1}$) is the precipitation rate.

Note that this method does not allow us to isolate within-column processes, including vertical mass exchanges through convective updrafts and downdrafts and through phase changes. We encourage future studies to isolate these within-column processes and establish how they evolve with topography.

3 Results

3.1 Model validation of ECHAM5-wiso

Under modern elevations, annual-mean precipitation-weighted $\delta^{18}O_p$ decreases with elevation on the Himalayan slope, increases with latitude across the Tibetan Plateau (Figs. 3a, 4), and varies little (mostly within 2‰) on the northern Tibetan slope (36–40° N; Fig. 4). Li et al. (2016) demonstrated that ECHAM5 simulates $\delta^{18}O$ variations across the Himalayas and the Tibetan Plateau that are in reasonable agreement with observed precipitation and stream values (see Sect. 2). Consistent with stream water samples, the model captures a decrease in $\delta^{18}O_p$ along a
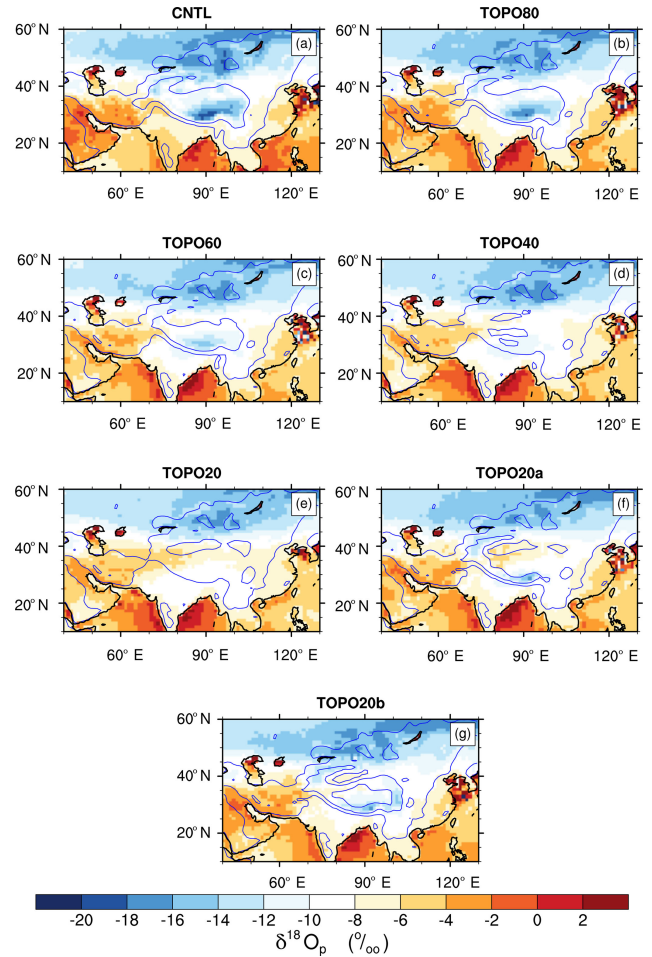
Figure 3. Mean-annual precipitation-weighted ECHAM $\delta^{18}O_p$ (in ‰) for the **(a)** CNTL, **(b)** TOPO80, **(c)** TOPO60, **(d)** TOPO40, **(e)** TOPO20, **(f)** TOPO20a, and **(g)** TOPO20b cases. The blue contour lines represent 500 and 2000 m surface elevation contours.

north–south transect across the Himalayas and an increase in $\delta^{18}O_p$ on the Tibetan Plateau (see their Fig. 12d). The main discrepancy occurs in winter and spring on the northwestern Tibetan Plateau. Simulated $\delta^{18}O_p$ is 4‰ greater than stream sample values along a cross section extending westward from 85° E and centered on 30° N. Li et al. (2016) attributed this mismatch to local factors, systematic model bias, and the influence of freshwater discharge from higher altitudes in the watershed.

We further compare ECHAM5 CNTL $\delta^{18}O_p$ with the modern surface water isotope dataset reported in Li and Garzione (2017) (Fig. 5). Colocated ECHAM and water sample $\delta^{18}O_p$ agree within 2‰ at 49.2 % of sites, and within 3‰ at 73.3 % of sites. Several discrepancies between simulated and observed $\delta^{18}O_p$ exist. Firstly, ECHAM5 $\delta^{18}O_p$ is lower than sampled $\delta^{18}O_p$ over northwestern Tibet (35–37° N, 80–85° E). This mismatch could be associated with the higher relative humidity in ECHAM (Fig. S1 in the Sup-
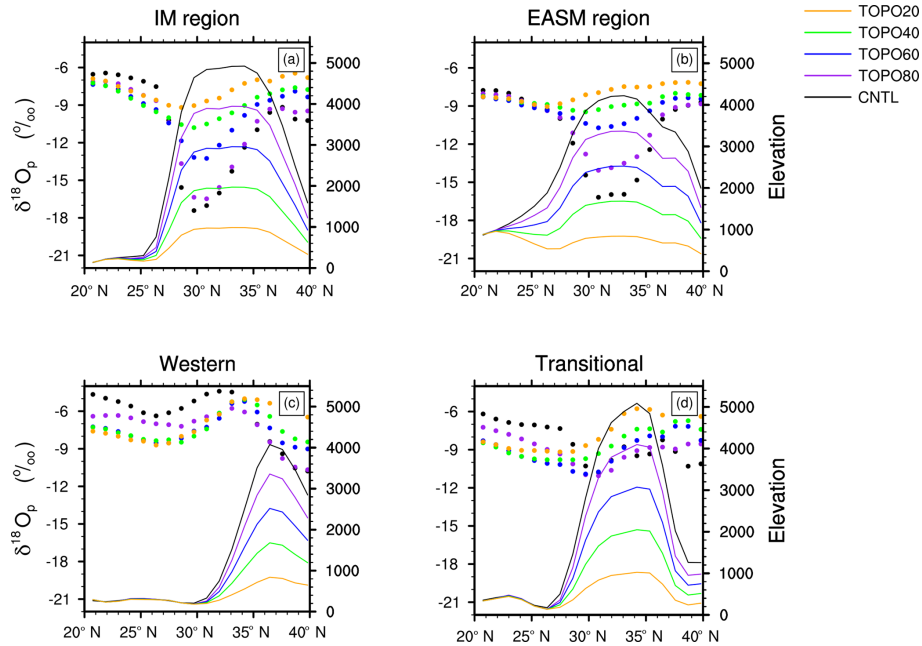
Figure 4. Annual-mean precipitation-weighted $\delta^{18}O_p$ (filled circles) and surface elevations (lines) along latitudinal transects for the **(a)** IM, **(b)** EASM, **(c)** western, and **(d)** transitional regions. These values represent zonal-average values over the specific region.

plement) than in the observations. This high relative humidity results in weaker evaporation both from land surface and below cloud-base, lowering $\delta^{18}O$ in surface waters. Secondly, ECHAM5 $\delta^{18}O_p$ is more depleted, by 2–5‰, over east-central Tibet (32–35° N, 89–102° E). The LMDZ-iso model shows a similar mismatch of 1–4‰ (Botsyun et al., 2016). In other regions of Tibet, simulated $\delta^{18}O_p$ values in LMDZ-iso are very similar to those in ECHAM5, within 2‰ (Yao et al., 2013). There are two potential explanations for the mismatch from modern surface water over east-central Tibet. One possibility is that the sampled $\delta^{18}O_p$ does not reflect mean climatic conditions. We note that the water samples from the east-central and northern Tibet regions were collected over a short 2-year span. This possibility is supported by the large interannual variability in $\delta^{18}O_p$ (up to 9‰) in both ECHAM (Li et al., 2016) and precipitation samples spanning the period from 1986 to 1992 from GNIP (IAEA/WMO, 2017). The other source for the mismatch over east-central Tibet is the higher than observed precipitation simulated by ECHAM5, which can result in lower $\delta^{18}O_p$ via the amount effect (as described in Sect. 3.6). The simulated summertime precipitation rate over east-central Tibet (32–35° N, 89–102° E) is 3.9 mm day^{-1}, which is higher than the 2.8 mm day^{-1} from Climate Prediction Center (CPC) Merged Analysis of Precipitation (CMAP) datasets (for 1981–2010). This high precipitation is systematic and is also seen in other models, such as LMDZ-iso (Botsyun et al., 2016) and ECHAM4 (Battisti et al., 2014).
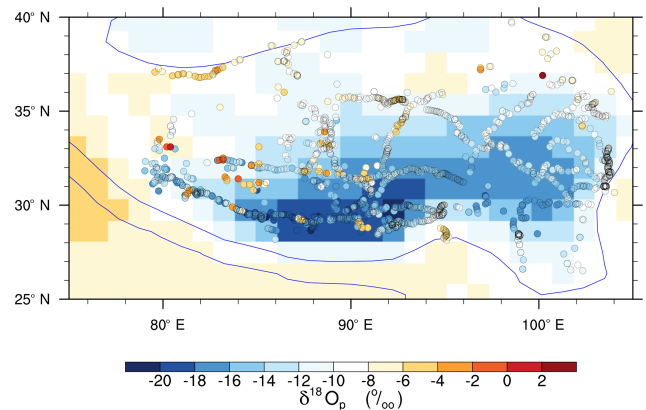

Figure 5. Comparison of annual-mean precipitation-weighted ECHAM $\delta^{18}O_p$ (shaded) with precipitation and stream samples (circles) from Li and Garzione (2017).

3.2 Climate response to Tibetan–Himalayan surface elevation

Numerous modeling studies have found that lowering the height of the Tibetan Plateau influences regional temperature, wind, precipitation, and relative humidity (e.g, Kitoh, 2004; Jiang et al., 2008). In this section, we describe regional climate changes on the western Himalayan slope, the Tibetan Plateau, the IM region, and the EASM region, which occur as high elevations are lowered.

Under modern conditions, near-surface temperatures in the Tibetan–Himalayan region vary with elevation following
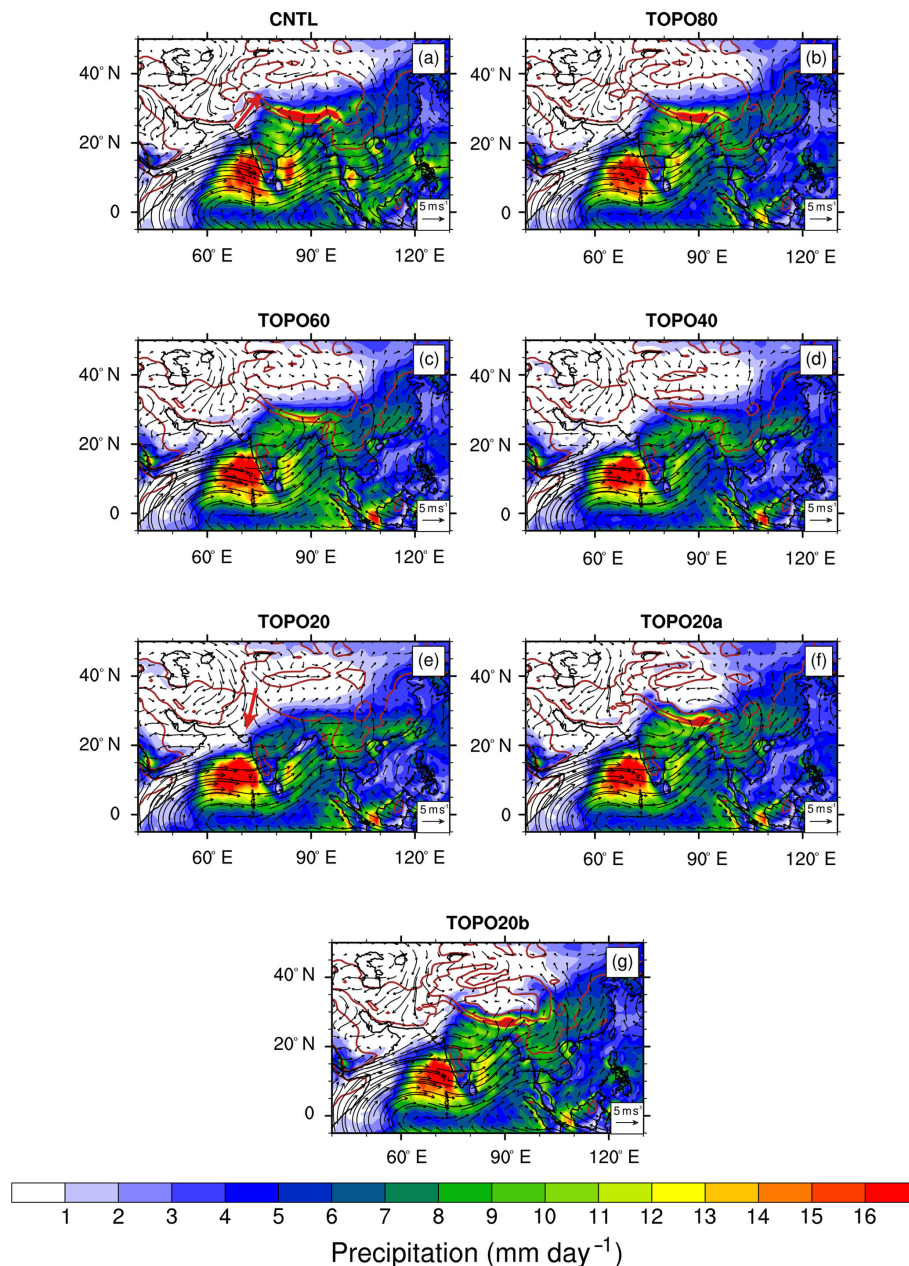
Figure 6. Summer (June–July–August) low-level (850 hPa) wind (arrows) and precipitation (shaded) for the **(a)** CNTL, **(b)** TOPO80, **(c)** TOPO60, **(d)** TOPO40, **(e)** TOPO20, **(f)** TOPO20a, and **(g)** TOPO20b cases. Brown contour lines represent 500 and 2000 m surface elevation contours in the Tibetan region. The red arrows on the western Himalayan slope in **(a)** and **(e)** show the wind direction reversal from CNTL to TOPO20.

a moist adiabatic lapse rate ($\sim 5\,°C\,km^{-1}$; Fig. S2) and range from $> 30\,°C$ on the Indian subcontinent at the foot of the Himalayas to $< 10\,°C$ across the Tibetan Plateau (Fig. S3a). Lowering elevations in our experiments causes near-surface temperatures across the Tibetan–Himalayan region to increase (Fig. S3b–g) at approximately the lapse rate for the CNTL case. As a result, temperature lapse rates vary little among elevation scenarios, for instance, ranging from 4.9 to $5.4\,°C\,km^{-1}$ in the IM region (Fig. 1).

Wind patterns, precipitation, and RH respond dramatically to reductions in elevation. These changes vary across regions. On the western Himalayan slope, wind directions nearly reverse with southerly winds in the high-elevation scenarios switching to northwesterly winds in low-elevation scenarios (Fig. 6). This wind reversal results in the transport of arid air from the north, which lowers total-column relative humidity by $\sim 40\,\%$. With this substantial decrease in RH, summer precipitation decreases from $\sim 3\,mm\,day^{-1}$ in the

CNTL to $\sim 0.1\,\mathrm{mm\,day^{-1}}$ on the western Himalayan slope in TOPO20. A similar decrease in RH, by $\sim 20\,\%$ from the CNTL to TOPO20, is simulated on the Tibetan Plateau. Accompanying this reduction in RH, precipitation on the Tibetan Plateau decreases from $\sim 4\,\mathrm{mm\,day^{-1}}$ in the CNTL to $\sim 1\,\mathrm{mm\,day^{-1}}$ in TOPO20. This reduction in Tibetan Plateau precipitation is linked to a weakening of the Asian monsoonal systems and moisture delivery through monsoonal winds.

The responses in the monsoonal regions are somewhat different from those on the western slope of the Himalayas and the Tibetan Plateau. A reduction in surface elevation (from CNTL to TOPO20; Fig. 1) leads to a weakening of the IM, as indicated by a slowing of summer southwesterly winds over the Bay of Bengal and the Arabian Sea and a decrease in summer precipitation (by more than $20\,\mathrm{mm\,day^{-1}}$ in ECHAM) along the central Himalayas (Fig. 6). IM weakening is also demonstrated by the WSI1 monsoon index (Fig. 7, following Wang and Fan, 1999), which is defined by the vertical wind shear between the lower (850 hPa) and upper (200 hPa) troposphere in the region (5–20° N, 40–80° E) during summer. Monthly WSI1 index values (not shown) indicate that the Indian monsoon persists through all elevation scenarios, although summertime WSI1 (Fig. 7) shows that it weakens abruptly once elevations are reduced to between 40 % and 60 % of modern values, a threshold reported in previous modeling studies (e.g., Abe et al., 2003). As a result of IM weakening, total-column average RH decreases from $> 90\,\%$ in CNTL to $70\,\%$ in TOPO20 and summer precipitation decreases from $> 16\,\mathrm{mm\,day^{-1}}$ in CNTL to $\sim 6\,\mathrm{mm\,day^{-1}}$ in TOPO20.

ECHAM5 captures a similar threshold behavior in monsoon activity in the EASM region. With lowering of the Himalayan front to 40 % of its modern elevations, the broad humid belt that characterizes central China in high-elevation scenarios (CNTL, TOPO80, TOPO60, TOPO20a, and TOPO20b) shifts southward, resulting in an expanded arid belt in the region (in TOPO40 and TOPO20). This shift in precipitation is associated with a southward retreat of the southwesterly monsoonal winds that penetrate much of eastern Asia (Fig. 6d, e).

3.3 Climate response to Himalayan surface elevation

ECHAM5 experiments TOPO20a and TOPO20b isolate the influence of Himalayan elevations on the regional climate. These experiments generally indicate that the Himalayas, rather than the Tibetan Plateau, govern regional precipitation and circulation patterns. The IM and EASM are strong in both TOPO20a and TOPO20b. The IM is shown by strong low-level wind over the Arabian Sea and heavy precipitation across both the Indian subcontinent and the central Himalayas in TOPO20a and TOPO20b (Fig. 6f, g). Likewise, the EASM in these simulations is similar to that in the CNTL as indicated by heavy precipitation to the north of the
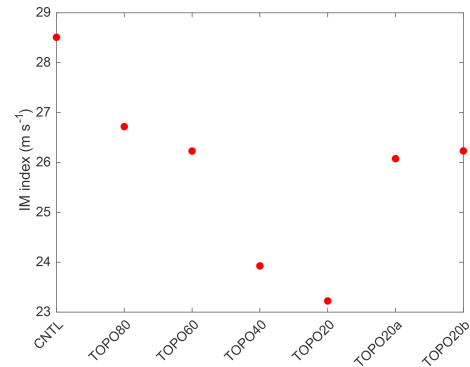
Figure 7. Indian summer monsoon (June–July–August) index, WSI1, calculated as the vertical wind shear between the lower (850 hPa) and upper (200 hPa) troposphere in the region (5–20° N, 40–80° E).

Yangtze River and southerly winds penetrating central China (Fig. 6f, g).

To further elucidate the contribution of the Himalaya to monsoonal dynamics, we calculated the equivalent potential temperature (Fig. S4), which is commonly used to denote the location of monsoonal heating for the Indian monsoon. In TOPO20a and TOPO20b, the equivalent potential temperature maxima are reduced but in a similar location to the CNTL case, supporting our conclusion that the Himalayas are the dominant driver of the IM. When the Himalayas are lowered, monsoonal heating decreases and the locus shifts southeastward as cold, dry extratropical air moves southward and mixes with warm, humid subcontinental air, consistent with the results in Boos (2015), although the extent of the shift is smaller in ECHAM5.

In contrast to this well established mechanism for the Indian monsoon, the mechanism for the southward shift of the EASM is not well understood. Uplift of the Himalaya–Tibet orogen (Guo et al., 2008; Liu et al., 2017), the retreat of the Paratethys (Guo et al., 2008), and forcing by atmospheric $p\mathrm{CO}_2$ (Licht et al., 2014; Caves Rugenstein and Chamberlain, 2018) have been proposed as possible factors triggering this southward shift, although the timing for the shift is highly debated from the Eocene to the early Miocene. Our simulation of a strong EASM over central China in both TOPO20a and TOPO20b suggests that uplift of the central and western Himalaya would have been capable of forcing this southward shift.

3.4 Moisture source influence on RDM δ^{18}O$_\mathrm{p}$

Under lower elevation scenarios, δ^{18}O$_\mathrm{p}$ values increase relative to the modern elevation scenario both on the Himalayas and the Tibetan Plateau (Fig. 4). The rate of change of δ^{18}O$_\mathrm{p}$ with elevation and latitude decreases substantially in the monsoonal regions as Tibetan–Himalayan elevations are reduced (Fig. 4a, b).

Table 1. Contribution of physical processes to annual-mean precipitation-weighted $\delta^{18}O_p$ (all units in ‰) averaged over monsoonal regions (IM and EASM). In the table, RDM_{ECHAM} represents the RDM initiated using the moisture sources (i.e., air temperature and relative humidity) from ECHAM5; RDM_{Fixed} is the $\delta^{18}O_p$ simulated by a RDM initiated with fixed moisture source of $T = 20\,^{\circ}C$ and RH = 80 %; and RDM_{Fixed_T} is initiated with fixed $T = 20\,^{\circ}C$ and ECHAM RH (refer to Sect. 2.2 for more details on the three different moisture sources). All columns show values averaged from mountain foot to mountain peak, except for the second column that shows the difference in $\delta^{18}O_p$ between mountain peak and foot as simulated by RDM_{ECHAM}.

| Case	RDM_{ECHAM} peak – foot (‰)	RDM_{ECHAM} – ECHAM5 (‰)	RDM_{Fixed} – RDM_{ECHAM} (‰)	RDM_{Fixed_T} – RDM_{ECHAM} (‰)	RDM_{Fixed} – RDM_{Fixed_T} (‰)
CNTL	−8.00	0.88	−0.32	−1.52	1.20
TOPO80	−6.15	1.89	1.73	−0.96	2.70
TOPO60	−4.16	1.80	2.25	−1.00	3.25
TOPO40	−2.53	0.86	2.34	−1.23	3.57
TOPO20	−1.12	−0.30	1.86	−1.51	3.37

The oxygen isotope compositions of precipitation on mountain slopes are traditionally assumed to systematically decrease in response to adiabatic cooling, condensation, and rainout of ascending air parcels, a process described by Rayleigh distillation and the basis for the application of $\delta^{18}O_p$ paleoaltimetry. In this section, we evaluate the degree to which Rayleigh distillation accounts for upslope decreases in $\delta^{18}O_p$ by comparing RDM to ECHAM $\delta^{18}O_p$ in four separate regions (Fig. 2). Note that the northern Tibetan slope is excluded here because most of the northerly air is diverted rather than being forced to ascend (Fig. 6).

For each of the four regions, we initialize the RDM with both fixed moisture sources (with initial $T = 20\,^{\circ}C$ and RH = 80 %) as in paleoaltimetry studies and with ECHAM moisture sources (with a T and RH that vary by region and case). The $\delta^{18}O_p$ predicted by the RDM using each moisture source is shown in Figs. 8 and 9 (red diamonds versus black circles). With ECHAM-derived T and RH, the RDM $\delta^{18}O_p$ values are close to those simulated by ECHAM5 in all elevation scenarios (Figs. 8, 9; Table 1, third column). RDM $\delta^{18}O_p$ with ECHAM-derived moisture is 0–2 ‰ less than that with fixed T and ECHAM RH (Table 1, fourth column), except in the CNTL scenario where the two RDM $\delta^{18}O_p$ are very close. The lower $\delta^{18}O_p$ is due to the fact that the RH of the initial air parcel is lower in ECHAM than in the prescribed case (Fig. S1). The impact of moisture source differences on $\delta^{18}O_p$ is further decomposed in Table 1 to estimate the contributions of adiabatic temperature versus RH changes. As seen in Table 3, the effect of adiabatic temperature changes is consistently small (~ -1 ‰) across all elevation scenarios, reflecting the fact that temperature lapse rates vary little among elevation scenarios (Fig. S2). In contrast, as the initial RH decreases with the lowering of elevation, ECHAM-sourced $\delta^{18}O_p$ is lowered by as much as 3.5 ‰ (Table 1, last column). In summary, these results demonstrate that elevation-related changes in moisture source characteristics substantially impact RDM $\delta^{18}O_p$ estimates.
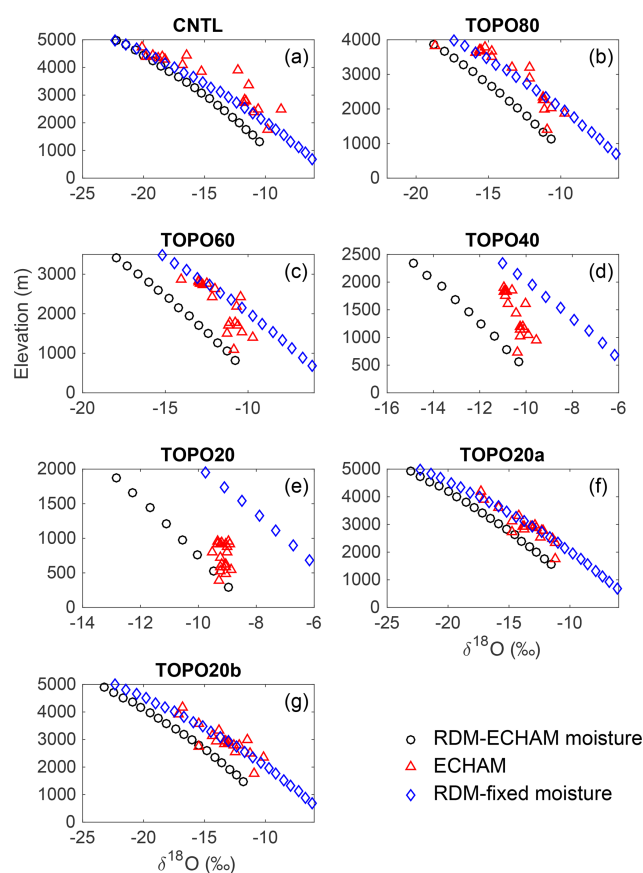
Figure 8. $\delta^{18}O_p$ (‰) versus elevation (m) for the Indian summer monsoon (ISM) region of the southern Himalayan flank as simulated by ECHAM5 (blue triangle, annual-mean precipitation-weighted), RDM initiated with ECHAM5 summertime moisture sources (black circle), and RDM initiated with fixed moisture sources of $T = 20\,^{\circ}C$ and RH = 80 % (red diamond) for the **(a)** CNTL, **(b)** TOPO80, **(c)** TOPO60, **(d)** TOPO40, **(e)** TOPO20, **(f)** TOPO20a, and **(g)** TOPO20b cases.
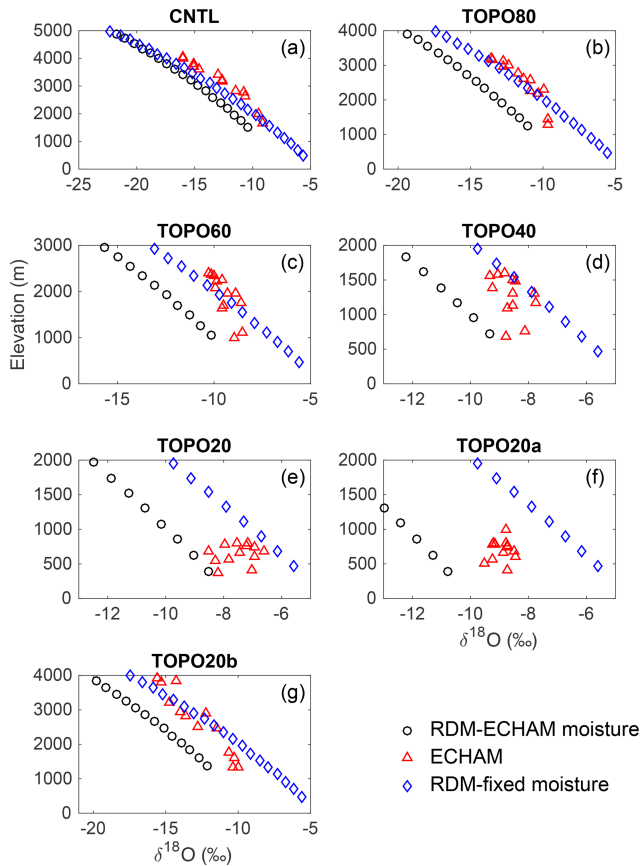
Figure 9. Same as in Fig. 7 but for the East Asian summer monsoon (EASM) region of the southern Himalayan flank.

3.5 Performance of ECHAM-sourced Rayleigh distillation in the Himalayas

Our estimates using an RDM implicitly assume that Rayleigh distillation is the dominant process controlling the δ^{18}O$_p$–elevation relationship. To test this assumption, we compare ECHAM-sourced RDM δ^{18}O$_p$ and ECHAM5 δ^{18}O$_p$.

Decreases in δ^{18}O$_p$ with elevation in ECHAM and the RDM generally agree under high-Himalaya scenarios and are consistent with modern observations (Table 2). Under modern topographic scenarios for the western Himalaya (Fig. S5) and the monsoonal regions (Figs. 8, 9), R^2 and p_percent values are greater than 0.77 and 0.51, respectively, indicating that RDM and ECHAM δ^{18}O$_p$ match well. R^2 and p_percent values are similarly high, above 0.68 and 0.53, respectively, for the western Himalaya and the monsoonal regions in the high-Himalaya scenarios (TOPO80, TOPO60, TOPO20a, and TOPO20b in the IM region; TOPO80 and TOPO20b in the EASM region) again indicating a good match between ECHAM and RDM δ^{18}O$_p$ and suggesting that Rayleigh distillation drives isotopic compositions in these regions.

In other regions and under low-elevation scenarios, however, the comparison between RDM and ECHAM δ^{18}O$_p$ is poor (Table 2). For instance, on the western Himalayas, in the TOPO80 case (Fig. S5), the lapse rate of ECHAM δ^{18}O$_p$ is much smaller than the lapse rate predicted by the RDM (Fig. S5), as shown by the p_percent values of less than 0.15. Under even lower elevation scenarios (TOPO60, TOPO40, and TOPO20), orographic precipitation is not triggered over the Himalayas (Fig. S4c–e), making the RDM an unsuitable representation of precipitation processes. In the transitional region, the δ^{18}O$_p$ can vary by more than 5 ‰ at a specific elevation under all elevation scenarios (Fig. S6). This large spread is represented by a low R^2 value of 0.12 for the CNTL case, and even lower values (less than 0.10) for other topographic scenarios. In TOPO40 and TOPO20, ECHAM δ^{18}O$_p$ shows little relationship with elevation (Fig. 4d).

In the monsoonal regions, the relationship between ECHAM5 δ^{18}O$_p$ and elevation is weak in low-elevation scenarios (Table 2, Fig. 4) and compares poorly with the RDM. In the IM region, p_percent values for the TOPO40 and TOPO20 are less than 0.29. In the EASM region, ECHAM5 δ^{18}O$_p$ is higher than RDM δ^{18}O$_p$ (Figs. 8, 9) in the TOPO60 scenario and the agreement is low (with a p_percent value of 0.31). Under even lower elevation scenarios (TOPO40 and TOPO20), ECHAM δ^{18}O$_p$ shows no relationship with elevation (Table 2, Fig. 4b) and also compares poorly with the RDM (with a p_percent value less than 0.29).

Among the high-Himalaya–low-Tibet cases (TOPO20a and TOPO20b), RDM and ECHAM δ^{18}O$_p$ match well in the IM region. The match is similarly good for TOPO20b in the EASM region. However, in the case with a low eastern flank (TOPO20a), the comparison is poor with an R^2 of 0.006 and a p_percent of -0.05.

3.6 Factors influencing the δ^{18}O$_p$–elevation relationship on the Himalayan slope

As shown in Sect. 3.5, Rayleigh distillation cannot explain δ^{18}O$_p$ variations with elevation for most regions in the reduced elevation (TOPO40 and TOPO20) scenarios and in many regions under higher elevation scenarios (TOPO80 and TOPO60). To understand the factors influencing δ^{18}O$_p$, we quantify the mass fluxes of ^{18}O (Fig. 10), distinguishing the processes that increase the mass flux of ^{18}O of the column (mixing and surface recycling) from those that decrease it (Rayleigh distillation and convective rainfall). Note that this method of taking the vertical column as a whole does not isolate the processes occurring within the air column (e.g., subcloud reevaporation, vertical advection, and mixing); this limitation does not impact our ability to identify the contributions of Rayleigh distillation and local processes. The results from this method yield very different contributions on the western slope from those in other regions; thus, the western Himalayas are reported separately.

Table 2. Summary of the comparison between ECHAM and RDM δ^{18}O$_p$ lapse rates under different topographic scenarios in different climate regions. Regions and scenarios with a high R^2 and p_percent are marked with an "X" indicating the existence of a significant δ^{18}O$_p$–elevation relationship (see methods in Sect. 2.2 for definitions of R^2 and p_percent).

Region	CNTL	TOPO80	TOPO60	TOPO40	TOPO20	TOPO20a	TOPO20b
Western	X					X	X
Transitional							
IM	X	X	X			X	X
EASM	X	X					X
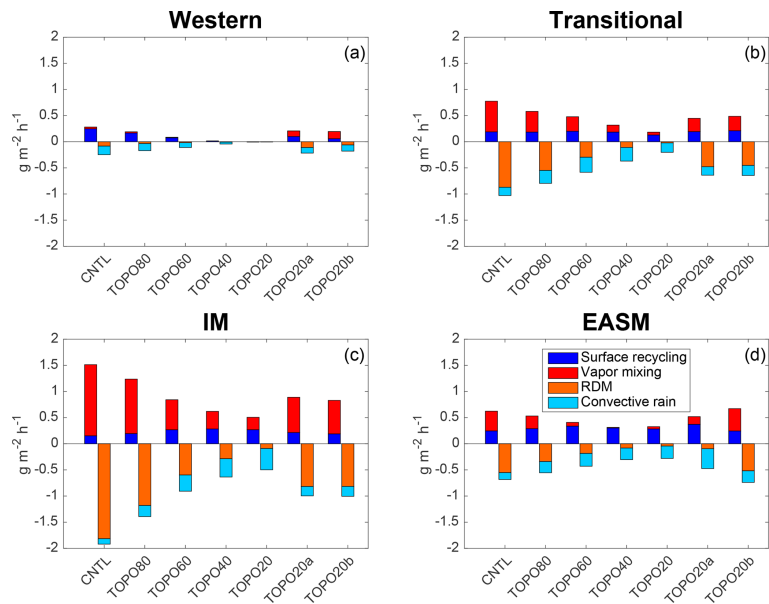
Figure 10. Summertime mass flux of ^{18}O (g m^{-2} h^{-1}) for the **(a)** western Himalayas, **(b)** the transitional, **(c)** the IM, and **(d)** the EASM regions. Sources (positive values) and sinks (negative values) balance within 20 % or 0.1 g m^{-2} h^{-1} for fluxes that are close to zero. (Small errors in the net balance arise due to the centered-finite-difference method used to calculate derivatives in the advection terms.) Note that the largest source/sink varies by region and with elevation. Local convection and surface recycling are the dominant respective source and sink of ^{18}O in the western Himalayas and under low-elevation scenarios, while Rayleigh distillation and vapor mixing dominate in high-elevation scenarios in the monsoonal and transitional regions.

On the western Himalayas, local surface recycling and convective rainfall contribute substantially to the total mass flux of ^{18}O$_p$ in the highest elevation scenarios (Fig. 10a). The contributions from these processes account for the poor match between RDM and ECHAM δ^{18}O$_p$ in this region. In the TOPO20a and TOPO20b scenarios, enhanced transport of enriched vapor from the south (see Fig. S7, 1 of 42 trajectories in CNTL versus 11 and 13 of 42 in TOPO20a and TOPO20b, respectively) increases the contribution from vapor mixing.

In the monsoonal regions and the transitional region, vapor mixing is the predominant source of ^{18}O under high-elevation scenarios and reflects the advection of ^{18}O-enriched vapor from the Arabian Sea and the Bay of Bengal. This mass flux of vapor mixing decreases substantially with a reduction in elevation, whereas the mass flux of surface recycling remains approximately constant in all elevation sce-

narios. As a result, surface recycling is as or more important than mixing as a source of ^{18}O under low-elevation scenarios (Fig. 10c, d). This change in the relative importance of the two sources represents an increase in the importance of local versus remote sources as monsoon strength weakens under low-elevation scenarios.

In high-elevation scenarios, Rayleigh distillation acts as the dominant sink of ^{18}O in the monsoonal regions causing δ^{18}O to decrease markedly with elevation (Fig. 10c, d). Under reduced elevation scenarios, the absolute mass flux from Rayleigh distillation decreases, as large-scale precipitation due to stable upslope ascent decreases and convective precipitation increases (Fig. 11). With reduced elevation, the percentage of large-scale precipitation to total precipitation falls from 86 % to 18 % in the transitional region, from 93 % to 18 % in the IM region, and from 80 % to 15 % in the EASM region, mirroring the decrease in the mass contribu-

Table 3. The isotopic contribution (in ‰) due to summertime sub-cloud reevaporation and surface recycling on the Tibetan Plateau for different elevation scenarios.

	CNTL	TOPO80	TOPO60	TOPO40	TOPO20
Sub-cloud reevaporation	9.06	10.02	7.97	5.21	5.28
Surface recycling	0.09	0.14	−1.40	−2.67	−1.8
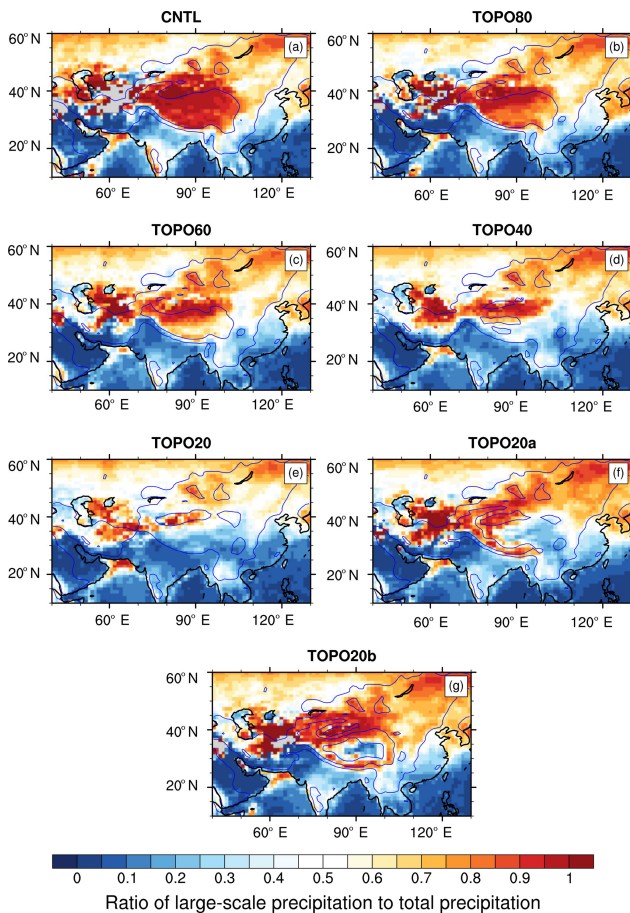
Figure 11. Ratio of summer large-scale to total precipitation rate in the **(a)** CNTL, **(b)** TOPO80, **(c)** TOPO60, **(d)** TOPO40, **(e)** TOPO20, **(f)** TOPO20a, and **(g)** TOPO20b cases. Blue lines mark the 500 and 2000 m elevation contours in each case. In the Himalayas, this ratio decreases when mountain elevations are reduced. As a result, large-scale precipitation is dominant in high-elevation scenarios, but not in low-elevation scenarios.

tion of Rayleigh distillation, which falls from 85 % to 11 % in the transitional region, from 93 % to 22 % in the IM region, and from 80 % to 18 % in the EASM region. As a result of the reduction in (large-scale) precipitation by stable upslope ascent, convective precipitation becomes the largest ^{18}O sink in TOPO20 and TOPO40 in both the transitional region and the IM region, and in TOPO60, TOPO40, TOPO20, and TOPO20a in the EASM region. These are also the scenarios that exhibited a poor match between RDM $\delta^{18}O_p$

and ECHAM $\delta^{18}O_p$ (Sect. 3.5). The increase in convective rainfall in these cases leads to greater kinetic fractionation through the sub-cloud evaporation of falling rain, which is only partially equilibrated with the surrounding vapor (see Sect. 2.1), and an enrichment in the isotopic composition of rain. The RDM does not capture this enrichment because it does not include sub-cloud evaporation. A similar reduction in large-scale precipitation with a reduction in elevation is also captured in the Andes region (Insel et al., 2009) and is associated with a decrease in the rate of change of $\delta^{18}O_p$ with elevation.
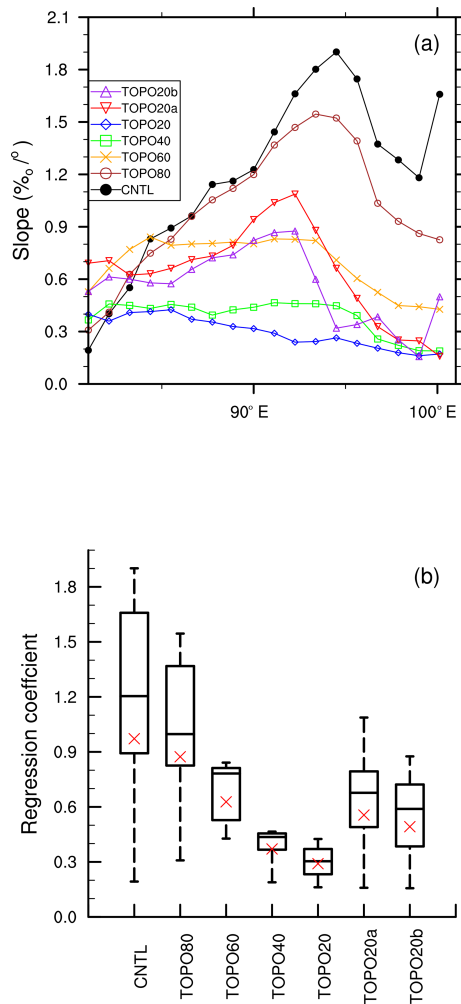
Note that, although Rayleigh distillation is the primary sink under high-elevation scenarios, RDM $\delta^{18}O_p$ does not match ECHAM $\delta^{18}O_p$ well in the transitional region because of the large spread in ECHAM $\delta^{18}O_p$ (Fig. S6). This spread is due to the bifurcated sources from northwest India (relatively enriched) and the Bay of Bengal (relatively depleted), as air parcels follow separate trajectories before mixing at the peak (Fig. S7).

In summary, the mismatch between RDM and ECHAM $\delta^{18}O_p$ is caused by a weakening of Rayleigh distillation under low-elevation scenarios, triggered by a reduction in large-scale precipitation.

3.7 $\delta^{18}O_p$–latitude relationship on the Tibetan Plateau

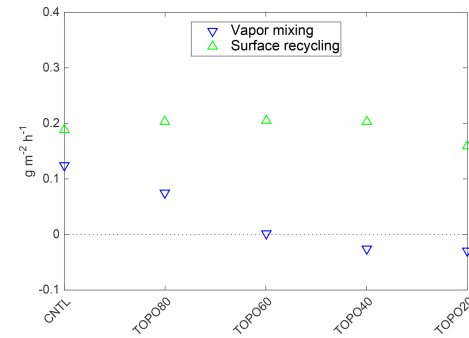In contrast to $\delta^{18}O_p$ on the Himalayas, $\delta^{18}O_p$ on the Tibetan Plateau increases linearly with latitude. It has been proposed that past $\delta^{18}O_p$, reconstructed from the isotopic analyses of ancient soil and lake carbonates, could provide information about past elevations on the Tibetan Plateau after removing the modern meridional $\delta^{18}O_p$ gradient (Bershaw et al., 2012). This proposal is problematic because the meridional $\delta^{18}O_p$ gradient and the processes that set this gradient on the Tibetan Plateau are poorly understood today and were likely different in the past in ways that are not known.

Tibetan Plateau meridional $\delta^{18}O_p$ gradients simulated by ECHAM5 under modern and reduced elevation scenarios are shown in Fig. 12. The average meridional gradient in the CNTL is 0.95 ‰ °$^{-1}$, which is very close to the observed gradient of 1.09 ‰ °$^{-1}$ (Li and Garzione, 2017). Three features of the latitudinal $\delta^{18}O_p$ gradients are notable. Firstly, the gradient varies with longitude (Fig 12a, b) and variations are larger in high-elevation cases (e.g., from 1.90 to 0.20 ‰ °$^{-1}$ in the CNTL). Secondly, a linear fit is generally good with a high coefficient of determination ($R^2 > 0.8$) east of 85° W

Figure 13. The mass flux of ^{18}O ($g\,m^{-2}\,h^{-1}$) from summertime (June–July–August) vapor mixing and surface recycling on the Tibetan Plateau. Note that the positive (negative) values indicate sources (sinks) of ^{18}O. Surface recycling is the largest source of ^{18}O under all elevation scenarios. Vapor mixing is secondary as a source in high-elevation scenarios and becomes a sink in low-elevation scenarios.
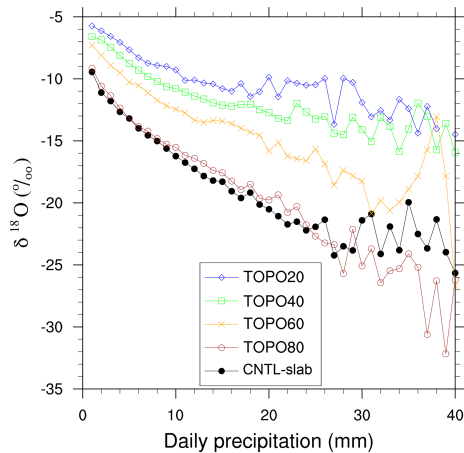
and varies little once the topography is lowered below the monsoon threshold in TOPO40 and TOPO20.

The modern latitudinal δ^{18}O$_p$ gradient on the Tibetan Plateau has been attributed to both surface recycling and sub-cloud reevaporation. Surface recycling increases δ^{18}O$_p$ by adding more enriched vapor from the land surface, while sub-cloud evaporation enriches ^{18}O in precipitation by partial evaporation of falling raindrops in an unsaturated air column. To understand the cause of the decline in the meridional δ^{18}O$_p$ gradient, we quantified both the sources of ^{18}O (surface recycling and vapor mixing) and the isotopic contribution due to sub-cloud reevaporation. Sub-cloud evaporation is quantified separately because this effect is contained in but cannot be isolated from the sources of ^{18}O.

Surface recycling is the primary source of ^{18}O on the Tibetan Plateau with largely consistent contributions under all elevation scenarios (Fig. 13). The mass flux of ^{18}O due to vapor mixing is small and becomes a sink in low-elevation scenarios, as there are increasingly more depleted sources from the south in these scenarios (e.g., 17 out of 42 in the CNTL versus 30 out of 42 in TOPO20 for one location – 33° N, 90° E). To further quantify the contribution of surface recycling to total precipitation, we subtracted δ^{18}O in precipitation from δ^{18}O in recycled vapor and normalized by the amount of precipitation and recycled vapor as in the following equation:

$$\left(\delta^{18}O_s - \delta^{18}O_p\right) \times E/P \times \rho_{water}, \qquad (7)$$

where δ^{18}O$_p$ is the isotopic composition in precipitation, δ^{18}O$_s$ is the condensate of recycled vapor, E ($m\,h^{-1}$) is the surface evaporation rate, and P ($m\,h^{-1}$) is the total precipitation rate. Results from Eq. (7) show that δ^{18}O of surface recycling contributes less than 0.1 ‰ in the CNTL and slightly more (-2.67 ‰) in TOPO20 (Table 3). The overall small contribution from surface recycling in ECHAM5 is due to the

Figure 12. (a) The slope (in $\%_o\,{}^{\circ-1}$) of the linear regression of annual-mean precipitation-weighted δ^{18}O$_p$ on latitude from ECHAM5 output, used as an approximation for the meridional gradient of δ^{18}O$_p$. **(b)** The box plot shows the variability of the meridional gradient of δ^{18}O$_p$. The red "x" indicates mean values for each scenario, calculated by regressing longitudinally averaged δ^{18}O$_p$ across the Tibetan Plateau on latitude. Box plots show minimum, maximum, median, and quartile values.

for all cases except TOPO20a and TOPO20b (Fig. S8). The high goodness of fit indicates a robust δ^{18}O$_p$–latitude relationship for the cases with uniform reductions in topography. The poor fit in TOPO20a and TOPO20b is due to the larger variations in elevation across the Tibetan Plateau. In these two cases, dry conditions (Fig. S1) on the steep leeward side of the Himalayas favor strong below cloud-base reevaporation, which increase local latitudinal δ^{18}O$_p$ gradients. Lastly, in cases with a uniform lowering of topography, the median meridional gradient (Fig. 12b) decreases almost linearly with reductions from 100 % to 60 % of modern topography, changes more abruptly between 60 % and 40 %,
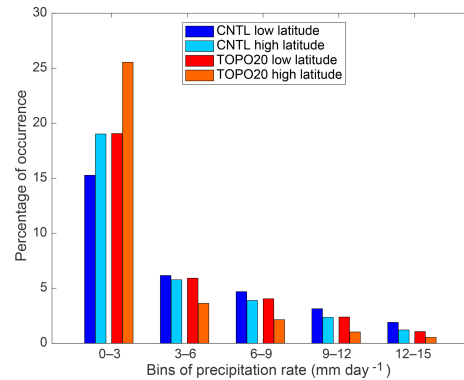
Figure 14. ECHAM $\delta^{18}O_p$ (‰) versus the daily summertime precipitation rate (mm day^{-1}) on the Tibetan Plateau. ECHAM $\delta^{18}O_p$ decreases with increasing precipitation under all elevation scenarios, but is greater in high-elevation scenarios than in low-elevation scenarios.

Figure 15. Relative occurrence (%) of summer daily precipitation rates on the Tibetan Plateau for lower latitudes (averaged over 30–32° N, 85–100° E) and higher latitudes (averaged over 34–36° N, 85–100° E). Only two elevation scenarios (CNTL and TOPO20) are shown here as the other scenarios are identical to these two. Low precipitation rate events are more frequent at higher latitudes than at lower latitudes under all elevation scenarios. See Fig. 13 for a demonstration of how this rainfall distribution impacts $\delta^{18}O_p$.

fact that δ^{18}O values in soil are similar to those in precipitation (Fig. S9). This small contribution grows in low-elevation scenarios due to the increased fraction of evaporated vapor to total precipitation (Fig. S10). Nonetheless, surface recycling plays a secondary role in decreasing the meridional $\delta^{18}O_p$ gradients.

Sub-cloud reevaporation occurs within an unsaturated air column as falling raindrops undergo kinetic fractionation and become isotopically enriched (Stewart, 1975). Enrichment is reduced in heavier rain where the relative humidity is high, resulting in the observed anticorrelation between $\delta^{18}O_p$ and the precipitation rate referred to as the amount effect. To quantify this enrichment due to sub-cloud reevaporation, we show $\delta^{18}O_p$ against daily precipitation (Fig. 14). The slope of this $\delta^{18}O_p$–precipitation relationship denotes the strength of the amount effect. In low-elevation scenarios, the $\delta^{18}O_p$–precipitation slope is shallower (Fig. 14), indicating a weaker amount effect and stronger sub-cloud reevaporation even at high precipitation rates.

This shallow sub-cloud evaporation slope results in the shallower meridional $\delta^{18}O_p$ gradient on the Tibetan Plateau in low-elevation scenarios. In each individual elevation scenario, the enrichment of $\delta^{18}O_p$ due to sub-cloud evaporation is stronger at higher latitudes as there are more instances of lower precipitation rates at higher latitudes than at lower latitudes (Fig. 15). As a result of this different distribution of precipitation, rainfall at higher latitudes is more enriched than that at lower latitudes. To further compare this contribution of sub-cloud reevaporation with surface recycling, the excess enrichment of $\delta^{18}O_p$ due to sub-cloud reevaporation is quantified by the $\delta^{18}O_p$ difference at high and low precipitation rates, weighted by precipitation rates (Table 3). The excess enrichment due to sub-cloud reevaporation is much

larger than that due to surface recycling and decreases with reduced elevation.

To explain this stronger sub-cloud reevaporation in low-elevation scenarios, we refer to the kinetic fractionation process in ECHAM5 during the partial evaporation of raindrops. As shown in Hoffmann et al. (1998), kinetic fractionation in ECHAM5 is formulated as follows:

$$\alpha = \frac{\text{RH}}{\frac{D}{\hat{D}}(\text{RH} - 1) + 1},\tag{8}$$

where α is the fractionation factor, $D \times \hat{D}^{-1}$ represents the ratio of diffusivities between ^{16}O and ^{18}O and has the constant value of 0.9727, and RH is the effective relative humidity of the grid box. To estimate how this kinetic fractionation changes between different elevation scenarios, we approximated the effective relative humidity to be the total-column-averaged RH. As seen in Fig. S11, the total-column-averaged RH at any given precipitation rate is higher in high-elevation scenarios than that in low-elevation scenarios. Specifically, when the precipitation rate is very high at 40 mm day^{-1}, the RH is at ~ 100 % in the CNTL, suggesting very little kinetic fractionation and weak sub-cloud reevaporation. In comparison, in TOPO20 the RH is much lower at ~ 85 %, indicating the presence of sub-cloud reevaporation even at high precipitation rates.

In summary, meridional $\delta^{18}O_p$ gradients on the Tibetan Plateau decrease with lower elevation, and this reduction is due to stronger sub-cloud evaporation in low-elevation scenarios.

4 Discussion

4.1 Processes impacting paleoaltimetry

The use of $\delta^{18}O_p$ as a paleoaltimeter is based on the principle that atmospheric vapor becomes saturated and condenses under forced ascent in orographic regions leading to the preferential rainout of ^{18}O. Observations of meteoric $\delta^{18}O$ in orographic regions support the use of stable isotope paleoaltimetry and show a robust and significant decreasing relationship in $\delta^{18}O_p$ with surface elevation (e.g., Poage and Chamberlain, 2001; Fiorella et al., 2015; Li and Garzione, 2017) that can be modeled by Rayleigh distillation (Rowley and Garzione, 2007). However, there is no a priori reason that modern $\delta^{18}O$–elevation relationships should hold in the past when surface elevations and associated atmospheric conditions were different (e.g., Ehlers and Poulsen, 2009; Poulsen et al., 2010; Feng et al., 2013; Botsyun et al., 2016).

Our ECHAM5 results confirm that the processes that govern $\delta^{18}O_p$ vary spatially and change in response to changes in surface elevation (Fig. 17). Across the Himalayan front, $\delta^{18}O_p$ generally decreases with elevation, particularly in scenarios with high Himalayan elevations. However, Rayleigh distillation often does a poor job of explaining the $\delta^{18}O_p$–elevation relationship in the Himalayan–Tibetan region. There are two primary reasons. Firstly, local processes including convection and surface recycling can dominate the land surface exchange of vapor (Fig. 10). These local processes are especially strong under low-elevation scenarios in monsoonal regions, where forced ascent is weak, and in the western Himalayas. Secondly, in regions with multiple moisture sources, the mixing of air masses with different $\delta^{18}O$ can cause the $\delta^{18}O_p$–elevation signal to deviate from that expected from Rayleigh distillation. The transitional region in the Himalayas, which receives moisture from both the Arabian Sea and the Bay of Bengal, is such a case (Fig. S7). On the Tibetan Plateau, the meridional $\delta^{18}O_p$ gradient decreases in response to reduced elevation. This meridional $\delta^{18}O_p$ gradient is primarily controlled by sub-cloud reevaporation under modern elevations. Sub-cloud reevaporation increases due to wetter conditions in low-elevation scenarios, reducing the meridional $\delta^{18}O_p$ gradient. Our conclusions are similar to those of Feng et al. (2013) for the North American Cordillera, in which it was shown that the isotopic fractionation of precipitation was not primarily due to Rayleigh distillation.

Our results also highlight the large influence that the choice of moisture source characteristics has on RDM $\delta^{18}O_p$ and are consistent with those of Botsyun et al. (2016). When we use fixed T and RH, ECHAM5 and RDM $\delta^{18}O_p$ agreement is poor with considerable enrichment in RDM. When we use ECHAM5 T and RH, the agreement is considerably improved. This change in moisture sources represents elevation-induced climate change unrelated to rainout and not captured by Rayleigh distillation. The overall impact
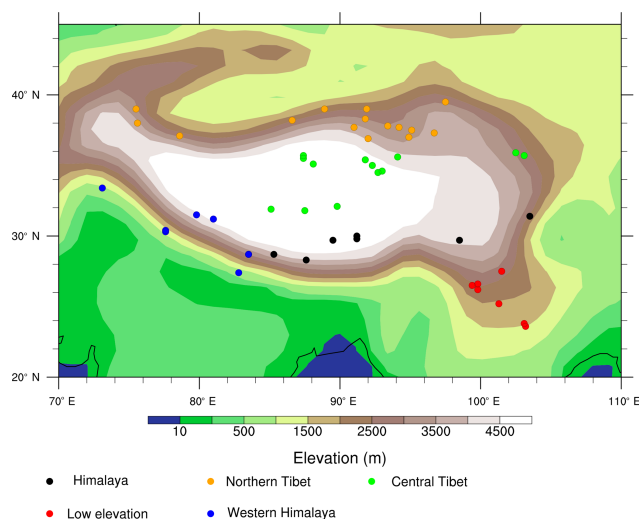

Figure 16. Map of $\delta^{18}O_p$ paleoaltimetry sites (filled circles) plotted on surface elevation (shaded). Sites are classified by their type (see Sect. 4.2 for more details on the categories and Table S1 for a list of the sites).

from T and RH (red diamonds in Figs. 8, 9) is a slight underestimation in high-elevation scenarios and a severe overestimation in low-elevation scenarios (e.g., by $\sim 100\%$ in TOPO20 in the IM region).

4.2 Implications for $\delta^{18}O_p$ paleoaltimetry

As discussed above, $\delta^{18}O_p$ paleoaltimetry is only appropriate for monsoonal regions in high-elevation scenarios. Nonetheless, proxy $\delta^{18}O_p$ from sites across the Himalayan–Tibetan region have been used to infer paleoaltimetry throughout the Cenozoic (Fig. 16, Table S1 in the Supplement). We classify these sites into five types indicating their utility for $\delta^{18}O_p$ paleoaltimetry.

As shown in Fig. 16 (black dots), the modern $\delta^{18}O_p$–elevation relationship is well captured by ECHAM5 and well represented by the Rayleigh distillation process under high-elevation scenarios for 7 of 50 sites located on the high Himalayas. However, for these seven sites, the $\delta^{18}O_p$–elevation relationship breaks down as the height of the Himalayan–Tibetan orogen is reduced. For 13 of 50 sites in central Tibet (green dots), there is no direct $\delta^{18}O_p$–elevation relationship, as elevation is largely uniform and $\delta^{18}O_p$ increases linearly with latitude due to sub-cloud reevaporation and recycling (as outlined in Sect. 3.7). Although it has been proposed that $\delta^{18}O_p$ paleoaltimetry is still possible after removing this meridional $\delta^{18}O_p$ gradient from $\delta^{18}O_p$ (Bershaw et al., 2012), the meridional gradient varies by as much as 70% with elevation and is largely unknown in the past (as shown in Sect. 3.7); thus, $\delta^{18}O_p$ paleoaltimetry is not appropriate for these sites. For 7 of 50 sites (red dots), elevations are too low, meaning that $\delta^{18}O_p$ has no relationship with elevation
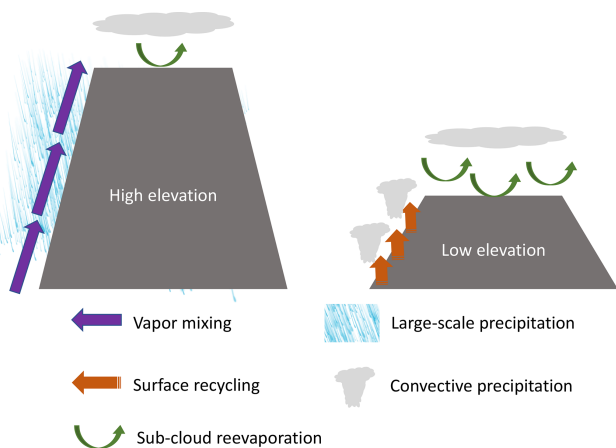
Figure 17. A sketch showing dominant sources/sinks of ^{18}O in the Himalayas and dominant process impacting δ^{18}O$_p$ on the Tibetan Plateau for high- and low-elevation scenarios.

and changes very little throughout different elevation scenarios (Fig. 4). As a result, δ^{18}O$_p$ is not indicative of elevation. For sites in the western and transitional regions (6 of 50), δ^{18}O$_p$ either relates very little to elevation or exhibits a large range at the same elevation (Fig. S6); thus, it is not appropriate for δ^{18}O$_p$ paleoaltimetry. Lastly, at sites in northern Tibet (yellow dots, 15 of 50), moisture is mostly diverted by the Tibetan Plateau, Rayleigh distillation is not triggered, and δ^{18}O$_p$ does not vary with elevation (Fig. 4).

Although the δ^{18}O$_p$–elevation relationship at sites in monsoonal regions (Fig. 16, black dots) are well explained by Rayleigh distillation in our experiments, δ^{18}O$_p$ paleoaltimetry should still be applied with care for these sites even under high-elevation conditions due to the influence of climate change. Proxy δ^{18}O$_p$ values as low as -18‰ to -16‰ are reported for the early Eocene (Ding et al., 2014) and around -14‰ for the late Eocene (Rowley and Currie, 2006). These values almost certainly reflect high elevations. Nonetheless, elevation-independent factors, including atmospheric pCO$_2$ (Poulsen and Jeffrey, 2011) and paleogeography (Roe et al., 2016), add substantial uncertainty to the quantification of past surface elevations.

4.3 Caveats

Like all models, ECHAM has limitations. Most pertinent to this study, ECHAM simulates higher precipitation along the steepest slope of a large mountain than indicated by satellite observations (Roe et al., 2016 and references therein), which is a common problem in most GCMs. The model tends to overestimate the modern precipitation amount and RH on the western Tibetan Plateau. This overestimation also exist in an earlier version of ECHAM (Roe et al., 2016) and in LMDZ-iso (Zhang and Li, 2016). The overestimation of total-column-averaged RH might weaken the sub-

cloud reevaporation process on the western plateau, and this weaker reevaporation could potentially lower the meridional δ^{18}O$_p$ gradient in this region. Another limitation of the model is that sub-grid scale lakes are not included. Although it has been proposed that the lakes provide δ^{18}O-enriched vapor to the air (Bershaw et al., 2012), under equilibrium conditions the net δ^{18}O flux to the air should be zero. Despite these limitations, ECHAM's simulation of δ^{18}O$_p$ compares favorably with natural water isotopic measurements (Li et al., 2016).

Another limitation of our modeling strategy is our use of a slab ocean model, which does not account for ocean circulation changes that would result from the changes in topography that we prescribe. To the best of our knowledge, no existing study has specifically investigated the response to a reduction in the elevations of the Himalayas and the Tibetan Plateau. It is not hard to imagine regional sea surface changes that might influence inland precipitation. For example, we speculate that under lower elevations and weaker monsoon winds, ocean upwelling along the western coast of the Bay of Bengal and the Arabian Sea would be reduced, leading to higher sea-surface temperatures (SSTs). In a study of the East Asian response to historical SST warming, higher SSTs led to greater precipitation over the Indian and Pacific oceans due to enhanced local convection and less precipitation along the Himalayan front, and further weakening of the Asian monsoon (Li et al., 2010). As this example highlights, future studies should incorporate dynamic ocean changes. An associated shortcoming is our prescription of fixed, mean-annual sea-surface δ^{18}O. To quantify this impact of the seasonal variations of seawater δ^{18}O on water vapor δ^{18}O, we estimated the seasonal change of water vapor δ^{18}O over the ocean using the Craig–Gordon model. Assuming a seasonal variation of 2.5‰ in sea water δ^{18}O (Breitenbach et al., 2010) and monthly SST, RH, and air temperature from our ECHAM5 CNTL case, we estimate that the seasonal change of water vapor δ^{18}O is within 0.3‰. This example illustrates the generally very small influence of seawater δ^{18}O variations on vapor and precipitation δ^{18}O.

In this study, we use a series of idealized simulations to investigate the response of water isotopes to mountain uplift and to understand the mechanisms that control δ^{18}O$_p$ variations in the Himalayas and on the Tibetan Plateau. We do not compare or evaluate our model results directly against proxies, as the simulations are not meant to represent specific time slices in the geologic past, and do not include changes in time-specific boundary conditions such as greenhouse gas composition, vegetation, orbital parameters (Tabor et al., 2018), glacial boundary conditions, tectonic displacement of the Indian subcontinent, or inclusion of the Paratethys. Changes in these boundary conditions, consistent with those that occurred through the Cenozoic, are likely to have a substantial influence on simulated δ^{18}O$_p$. For instance, high early Cenozoic atmospheric CO$_2$ may have increased δ^{18}O$_p$ over high-elevation regions (Jeffery et al., 2012; Poulsen and Jeffery, 2011) and on the Tibetan Plateau

by as much as 8‰ (Poulsen and Jeffery, 2011). In addition, Earth's orbital variations have been shown to contribute as much as 7‰ to oxygen isotope changes on the Tibetan Plateau (Battisti et al., 2014), which is comparable to the isotope difference from the CNTL to TOPO20 (about -11‰) in Fig. 4. These large variations associated with orbital fluctuations are not observed in long records spanning millions of years (Deng and Ding, 2015; Kent-Corson et al., 2009), presumably because the terrestrial proxy archives of δ^{18}O integrate over orbital time periods.

5   Conclusion

The isotopic composition of ancient meteoric waters archived in terrestrial proxies is often used as a paleoaltimeter under the assumption that rainout during stable air parcel ascent over topography leads to a systemic isotopic depletion via Rayleigh distillation. We use an isotope-enabled GCM, ECHAM5-wiso, to evaluate the extent to which oxygen isotopes can be used as a paleoaltimeter for the Himalayan–Tibetan region and to explore the processes that control the δ^{18}O–elevation relationship. Overall, our study highlights the myriad processes that influence $\delta^{18}O_p$ in the Himalayan–Tibetan region now and during its uplift.

We find that Rayleigh distillation describes most of the $\delta^{18}O_p$ variation with elevation in the monsoonal regions under high-topography scenarios. In contrast, Rayleigh distillation does a poor job of describing $\delta^{18}O_p$ variation with elevation under high-topography scenarios in the western Himalayas due to the dominance of local convection and surface recycling in the region. When the Himalayan–Tibetan elevations are reduced to below one-half of their modern heights, $\delta^{18}O_p$ exhibits no relationship with elevation. At these reduced elevations, δ^{18}O fractionation occurs primarily through local convection and surface recycling. On the Tibetan Plateau under modern elevations conditions, $\delta^{18}O_p$ linearly increases with latitude primarily due to sub-cloud reevaporation. The $\delta^{18}O_p$ gradient decreases as the plateau is lowered due primarily to stronger sub-cloud reevaporation under drier conditions and secondarily owing to increased moisture sources from surface recycling. Because of these elevation-independent processes, we conclude that only 7 out of the 50 paleoaltimetry sites are appropriate for δ^{18}O paleoaltimetry. Taken together, these results indicate that stable isotope paleoaltimetry in the Himalayan–Tibetan region, as in other orogenic regions, is at best a blunt instrument for inferring past surface elevations.

References

Abe, M., Kitoh, A., and Yasunari, T.: An Evolution of the Asian Summer Monsoon Associated with Mountain Uplift – Simulation with the MRI Atmosphere–Ocean Coupled GCM, J. Meteorol. Soc. Jpn. Ser. II, 81, 909–933, https://doi.org/10.2151/jmsj.81.909, 2003.

Antonelli, A., Kissling, W. D., Flantua, S. G. A., Bermúdez, M. A., Mulch, A., Muellner-Riehl, A. N., Kreft, H., Linder, H. P., Badgley, C., Fjeldså, J., Fritz, S. A., Rahbek, C., Herman, F., Hooghiemstra, H., and Hoorn, C.: Geological and climatic influences on mountain biodiversity, Nat. Geosci., 11, 718–725, https://doi.org/10.1038/s41561-018-0236-z, 2018.

Aron, P. G. and Poulsen, C. J.: Cenozoic mountain building and climate evolution, in: Mountains, Climate and Biodiversity, John Wiley and Sons Ltd, New York, 111–121, 2018.

Battisti, D. S., Ding, Q., and Roe, G. H.: Coherent pan-Asian climatic and isotopic response to orbital forcing of tropical insolation, J. Geophys. Res.-Atmos., 119, 11997–12020, https://doi.org/10.1002/2014JD021960, 2014.

Bershaw, J., Penny, S. M., and Garzione, C. N.: Stable isotopes of modern water across the Himalaya and eastern Tibetan Plateau: Implications for estimates of paleoelevation and paleoclimate, J. Geophys. Res.-Atmos., 117, D02110, https://doi.org/10.1029/2011jd016132, 2012.

Boos, W. R.: A review of recent progress on Tibet's role in the South Asian monsoon, CLIVAR Exchanges Special Issue on Monsoons, 66, 23–27, 2015.

Boos, W. R. and Kuang, Z.: Dominant control of the South Asian monsoon by orographic insulation versus plateau heating, Nature, 463, 218–222, https://doi.org/10.1038/nature08707, 2010.

Botsyun, S., Sepulchre, P., Risi, C., and Donnadieu, Y.: Impacts of Tibetan Plateau uplift on atmospheric dynamics and associated precipitation δ^{18}O, Clim. Past, 12, 1401–1420, https://doi.org/10.5194/cp-12-1401-2016, 2016.

Breitenbach, S. F. M., Adkins, J. F., Meyer, H., Marwan, N., Kumar, K. K., and Haug, G. H.: Strong influence of water vapor source dynamics on stable isotopes in precipitation observed in South-

ern Meghalaya, NE India, Earth Planet. Sc. Lett., 292, 212–220, https://doi.org/10.1016/j.epsl.2010.01.038, 2010.

Caves Rugenstein, J. K. and Chamberlain, C. P.: The evolution of hydroclimate in Asia over the Cenozoic: A stable-isotope perspective, Earth-Sci. Rev., 185, 1129–1156, https://doi.org/10.1016/j.earscirev.2018.09.003, 2018.

Chamberlain, C. P. and Poage, M. A.: Reconstructing the paleotopography of mountain belts from the isotopic composition of authigenic minerals, Geology, 28, 115–118, https://doi.org/10.1130/0091-7613(2000)28<115:RTPOMB>2.0.CO;2, 2000.

Cyr, A. J., Currie, B. S., and Rowley, D. B.: Geochemical evaluation of Fenghuoshan Group lacustrine carbonates, North-Central Tibet: Implications for the paleoaltimetry of the Eocene Tibetan Plateau, J. Geol., 113, 517–533, https://doi.org/10.1086/431907, 2005.

Deng, T. and Ding, L.: Paleoaltimetry reconstructions of the Tibetan Plateau: progress and contradictions, Nat. Sci. Rev., 2, 417–437, https://doi.org/10.1093/nsr/nwv062, 2015.

Ding, L., Xu, Q., Yue, Y., Wang, H., Cai, F., and Li, S.: The Andean-type Gangdese Mountains: Paleoelevation record from the Paleocene–Eocene Linzhou Basin, Earth Planet. Sc. Lett., 392, 250–264, https://doi.org/10.1016/j.epsl.2014.01.045, 2014.

Ehlers, T. A. and Poulsen, C. J.: Influence of Andean uplift on climate and paleoaltimetry estimates, Earth Planet. Sc. Lett., 281, 238–248, https://doi.org/10.1016/j.epsl.2009.02.026, 2009.

Fan, M., Heller, P., Allen, S. D., and Hough, B. G.: Middle Cenozoic uplift and concomitant drying in the central Rocky Mountains and adjacent Great Plains, Geology, 42, 547–550, https://doi.org/10.1130/G35444.1, 2014.

Feng, R. and Poulsen, C. J.: Refinement of Eocene lapse rates, fossil-leaf altimetry, and North American Cordilleran surface elevation estimates, Earth Planet. Sc. Lett., 436, 130–141, https://doi.org/10.1016/j.epsl.2015.12.022, 2016.

Feng, R., Poulsen, C. J., Werner, M., Chamberlain, C. P., Mix, H. T., and Mulch, A.: Early Cenozoic evolution of topography, climate, and stable isotopes in precipitation in the North American Cordillera, Am. J. Sci., 313, 613–648, https://doi.org/10.2475/07.2013.01, 2013.

Fiorella, R. P., Poulsen, C. J., Pillco Zolá, R. S., Jeffery, M. L., and Ehlers, T. A.: Modern and long-term evaporation of central Andes surface waters suggests paleo archives underestimate Neogene elevations, Earth Planet Sc. Lett., 432, 59–72, https://doi.org/10.1016/j.epsl.2015.09.045, 2015.

Galy, V., France-Lanord, C., Beyssac, O., Faure, P., Kudrass, H., and Palhol, F.: Efficient organic carbon burial in the Bengal fan sustained by the Himalayan erosional system, Nature, 450, 407–410, https://doi.org/10.1038/nature06273, 2007.

Garzione, C. N., Hoke, G. D., Libarkin, J. C., Withers, S., MacFadden, B., Eiler, J., Ghosh, P., and Mulch, A.: Rise of the Andes, Science, 320, 1304–1307, https://doi.org/10.1126/science.1148615, 2008.

Gleckler, P.: The Second Phase of the Atmospheric Model Intercomparison Project (AMIP2), Lawrence Livermore National Lab., Livermore, CA, USA, 2005.

Guo, Z. T., Sun, B., Zhang, Z. S., Peng, S. Z., Xiao, G. Q., Ge, J. Y., Hao, Q. Z., Qiao, Y. S., Liang, M. Y., Liu, J. F., Yin, Q. Z., and Wei, J. J.: A major reorganization of Asian climate by the early

Miocene, Clim. Past, 4, 153–174, https://doi.org/10.5194/cp-4-153-2008, 2008.

Haese, B., Werner, M., and Lohmann, G.: Stable water isotopes in the coupled atmosphere-land surface model ECHAM5-JSBACH, Geosci. Model Dev., 6, 1463–1480, https://doi.org/10.5194/gmd-6-1463-2013, 2013.

Hoffmann, G., Werner, M., and Heimann, M.: Water isotope module of the ECHAM atmospheric general circulation model: A study on timescales from days to several years, J. Geophys. Res.-Atmos., 103, 16871–16896, https://doi.org/10.1029/98JD00423, 1998.

Hoke, G. D., Liu-Zeng, J., Hren, M. T., Wissink, G. K., and Garzione, C. N.: Stable isotopes reveal high southeast Tibetan Plateau margin since the Paleogene, Earth Planet. Sc. Lett., 394, 270–278, https://doi.org/10.1016/j.epsl.2014.03.007, 2014.

IAEA/WMO: Global Network of Isotopes in Precipitation, The GNIP Database, available at: http://www.iaea.org/water (last access: January 2019), 2017.

Insel, N., Poulsen, C. J., and Ehlers, T. A.: Influence of the Andes Mountains on South American moisture transport, convection, and precipitation, Clim. Dynam., 35, 1477–1492, https://doi.org/10.1007/s00382-009-0637-1, 2009.

Jeffery, M. L., Poulsen, C. J., and Ehlers, T. A.: Impacts of Cenozoic global cooling, surface uplift, and an inland seaway on South American paleoclimate and precipitation δ^{18}O, GSA Bulletin, 124, 335–351, https://doi.org/10.1130/B30480.1, 2012.

Jiang, D., Ding, Z., Drange, H., and Gao, Y.: Sensitivity of East Asian climate to the progressive uplift and expansion of the Tibetan Plateau under the mid-Pliocene boundary conditions, Adv. Atmos. Sci., 25, 709–722, https://doi.org/10.1007/s00376-008-0709-x, 2008.

Kent-Corson, M. L., Ritts, B. D., Zhuang, G., Bovet, P. M., Graham, S. A., and Page Chamberlain, C.: Stable isotopic constraints on the tectonic, topographic, and climatic evolution of the northern margin of the Tibetan Plateau, Earth Planet. Sc. Lett., 282, 158–166, https://doi.org/10.1016/j.epsl.2009.03.011, 2009.

Kitoh, A.: Effects of Mountain Uplift on East Asian Summer Climate Investigated by a Coupled Atmosphere–Ocean GCM, J. Climate, 17, 783–802, https://doi.org/10.1175/1520-0442(2004)017<0783:EOMUOE>2.0.CO;2, 2004.

Kutzbach, J. E., Guetter, P. J., Ruddiman, W. F., and Prell, W. L.: Sensitivity of climate to late Cenozoic uplift in southern Asia and the American west: Numerical experiments, J. Geophys. Res.-Atmos., 94, 18393–18407, https://doi.org/10.1029/JD094iD15p18393, 1989.

LeGrande, A. N. and Schmidt, G. A.: Global gridded data set of the oxygen isotopic composition in seawater, Geophys. Res. Lett., 33, L12604, https://doi.org/10.1029/2006GL026011, 2006.

Li, H., Dai, A., Zhou, T., and Lu, J.: Responses of East Asian summer monsoon to historical SST and atmospheric forcing during 1950–2000, Clim. Dynam., 34, 501–514, https://doi.org/10.1007/s00382-008-0482-7, 2010.

Li, J., Ehlers, T. A., Mutz, S. G., Steger, C., Paeth, H., Werner, M., Poulsen, C. J., and Feng, R.: Modern precipitation δ^{18}O and trajectory analysis over the Himalaya–Tibet Orogen from ECHAM5-wiso simulations, J. Geophys. Res.-Atmos., 121, 10432–10452, https://doi.org/10.1002/2016JD024818, 2016.

Li, L. and Garzione, C.: Spatial distribution and controlling factors of stable isotopes in meteoric waters on the Tibetan Plateau:

implications for paleoelevation reconstruction, Earth Planet. Sc. Lett., 302–314, https://doi.org/10.1016/j.epsl.2016.11.046, 2017.

Li, S., Currie, B. S., Rowley, D. B., and Ingalls, M.: Cenozoic paleoaltimetry of the SE margin of the Tibetan Plateau: Constraints on the tectonic evolution of the region, Earth Planet. Sc. Lett., 432, 415–424, https://doi.org/10.1016/j.epsl.2015.09.044, 2015.

Licht, A., van Cappelle, M., Abels, H. A., Ladant, J. B., Trabucho-Alexandre, J., France-Lanord, C., Donnadieu, Y., Vandenberghe, J., Rigaudier, T., Lecuyer, C., Terry Jr, D., Adriaens, R., Boura, A., Guo, Z., Soe, A. N., Quade, J., Dupont-Nivet, G., and Jaeger, J. J.: Asian monsoons in a late Eocene greenhouse world, Nature, 513, 501–506, https://doi.org/10.1038/nature13704, 2014.

Liu, X., Dong, B., Yin, Z.-Y., Smith, R. S., and Guo, Q.: Continental drift and plateau uplift control origination and evolution of Asian and Australian monsoons, Scient. Rep., 7, 40344, https://doi.org/10.1038/srep40344, 2017.

Maffre, P., Ladant, J.-B., Moquet, J.-S., Carretier, S., Labat, D., and Goddéris, Y.: Mountain ranges, climate and weathering. Do orogens strengthen or weaken the silicate weathering carbon sink?, Earth Planet. Sc. Lett., 493, 174–185, https://doi.org/10.1016/j.epsl.2018.04.034, 2018.

Peters, N. A., Huntington, K. W., and Hoke, G. D.: Hot or not? Impact of seasonally variable soil carbonate formation on paleotemperature and O-isotope records from clumped isotope thermometry, Earth Planet. Sc. Lett., 361, 208–218, https://doi.org/10.1016/j.epsl.2012.10.024, 2013.

Poage, M. A. and Chamberlain, C. P.: Empirical Relationships Between Elevation and the Stable Isotope Composition of Precipitation and Surface Waters: Considerations for Studies of Paleoelevation Change, Am. J. Sci., 301, 1–15, https://doi.org/10.2475/ajs.301.1.1, 2001.

Poage, M. A. and Chamberlain, C. P.: Stable isotopic evidence for a Pre-Middle Miocene rain shadow in the western Basin and Range: Implications for the paleotopography of the Sierra Nevada, Tectonics, 21, 16-1–16-10, https://doi.org/10.1029/2001TC001303, 2002.

Poulsen, C. J. and Jeffery, M. L.: Climate change imprinting on stable isotopic compositions of high-elevation meteoric water cloaks past surface elevations of major orogens, Geology, 39, 595–598, https://doi.org/10.1130/g32052.1, 2011.

Poulsen, C. J., Ehlers, T. A., and Insel, N.: Onset of convective rainfall during gradual late Miocene rise of the central Andes, Science, 328, 490–493, https://doi.org/10.1126/science.1185078, 2010.

Quade, J., Breecker, D. O., Daeron, M., and Eiler, J.: The paleoaltimetry of Tibet: An isotopic perspective, Am. J. Sci., 311, 77–115, https://doi.org/10.2475/02.2011.01, 2011.

Roe, G. H., Ding, Q., Battisti, D. S., Molnar, P. H., Clark, M. K., and Garzione, C.: A modeling study of the response of Asian summertime climate to the largest geologic forcings of the past 50 Ma, J. Geophys. Res.-Atmos., 121, 5453–5470, https://doi.org/10.1002/2015JD024370, 2016.

Rohrmann, A., Kapp, P., Carrapa, B., Reiners, P. W., Guynn, J., Ding, L., and Heizler, M.: Thermochronologic evidence for plateau formation in central Tibet by 45 Ma, Geology, 40, 187–190, https://doi.org/10.1130/G32530.1, 2012.

Rowley, D. B. and Currie, B. S.: Palaeo-altimetry of the late Eocene to Miocene Lunpola basin, central Tibet, Nature, 439, 677–681, https://doi.org/10.1038/nature04506, 2006.

Rowley, D. B. and Garzione, C. N.: Stable Isotope-Based Paleoaltimetry, Annu. Rev. Earth Planet. Sci., 35, 463–508, https://doi.org/10.1146/annurev.earth.35.031306.140155, 2007.

Rowley, D. B., Pierrehumbert, R. T., and Currie, B. S.: A new approach to stable isotope-based paleoaltimetry: implications for paleoaltimetry and paleohypsometry of the High Himalaya since the Late Miocene, Earth Planet. Sc. Lett., 188, 253–268, https://doi.org/10.1016/s0012-821x(01)00324-7, 2001.

Royden, L. H., Burchfiel, B. C., and van der Hilst, R. D.: The Geological Evolution of the Tibetan Plateau, Science, 321, 1054–1058, https://doi.org/10.1126/science.1155371, 2008.

Stewart, M. K.: Stable isotope fractionation due to evaporation and isotopic exchange of falling waterdrops: Applications to atmospheric processes and evaporation of lakes, J. Geophys. Res., 80, 1133–1146, https://doi.org/10.1029/JC080i009p01133, 1975.

Tabor, C. R., Otto-Bliesner, B. L., Brady, E. C., Nusbaumer, J., Zhu, J., Erb, M. P., Wong, T. E., Liu, Z., and Noone, D.: Interpreting Precession-Driven δ^{18}O Variability in the South Asian Monsoon Region, J. Geophys. Res.-Atmos., 123, 5927–5946, https://doi.org/10.1029/2018JD028424, 2018.

Wang, B. and Fan, Z.: Choice of South Asian Summer Monsoon Indices, B. Am. Meteorol. Soc., 80, 629–638, https://doi.org/10.1175/1520-0477(1999)080<0629:COSASM>2.0.CO;2, 1999.

Yang, S., Dong, H., and Lei, F.: Phylogeography of regional fauna on the Tibetan Plateau: A review, Prog. Nat. Sci., 19, 789–799, https://doi.org/10.1016/j.pnsc.2008.10.006, 2009.

Yao, T. D., Masson-Delmotte, V., Gao, J., Yu, W. S., Yang, X. X., Risi, C., Sturm, C., Werner, M., Zhao, H. B., He, Y., Ren, W., Tian, L. D., Shi, C. M., and Hou, S. G.: A review of climatic controls on δ^{18}O in precipitation over the Tibetan Plateau: observations and simulations, Rev. Geophys., 51, 525–548, https://doi.org/10.1002/rog.20023, 2013.

Zhang, R., Jiang, D., Zhang, Z., and Yu, E.: The impact of regional uplift of the Tibetan Plateau on the Asian monsoon climate, Palaeogeogr. Palaeocl., 417, 137–150, https://doi.org/10.1016/j.palaeo.2014.10.030, 2015.

Zhang, Y. and Li, J.: Impact of moisture divergence on systematic errors in precipitation around the Tibetan Plateau in a general circulation model, Clim. Dynam., 47, 2923–2934, https://doi.org/10.1007/s00382-016-3005-y, 2016.

Zhao, J., Xia, Y., Cannon, C. H., Kress, W. J., and Li, Q.: Evolutionary diversification of alpine ginger reflects the early uplift of the Himalayan–Tibetan Plateau and rapid extrusion of Indochina, Gondwana Res., 32, 232–241, https://doi.org/10.1016/j.gr.2015.02.004, 2016.